# Interseismic deformation and strain-partitioning along the Main Köpetdag Fault, Turkmenistan, with Sentinel-1 InSAR time-series

N. Dodds, S. Daout, R. T. Walker, G. Begenjev, Y. Bezmenov, R. Mirzin, B. Parsons

Geophysical Journal International

*Geophys. J. Int.* (2022) **230,** 1612–1629
Advance Access publication 2022 April 15
GJI Geodynamics and Tectonics

https://doi.org/10.1093/gji/ggac139

# Interseismic deformation and strain-partitioning along the Main Köpetdag Fault, Turkmenistan, with Sentinel-1 InSAR time-series

N. Dodds [1], S. Daout,[1,2] R.T. Walker [1], G. Begenjev,[3] Y. Bezmenov,[3] R. Mirzin[3] and B. Parsons[1]

[1] *COMET, Department of Earth Sciences, Oxford University, Oxford OX*1 2*JD, UK. E-mail: nick.w.dodds@gmail.com*
[2] *CRPG, Université de Lorraine - CNRS,* 54500 *Vandœuvre-lès-Nancy, France*
[3] *Institute of Seismology and Atmospheric Physics, Academy of Sciences of Turkmenistan, Aşgabat* 744000*, Turkmenistan*

Accepted 2022 April 4. Received 2022 March 31; in original form 2021 July 27

## SUMMARY

The Main Köpetdag Fault (MKDF) is a predominantly right-lateral strike-slip fault that dissects the northern edge of the Köpetdag mountains of Turkmenistan and Iran. The fault represents the northernmost expression of deformation from the Arabia–Eurasia collision to the east of the Caspian Sea, and plays an important role facilitating the motion of the South Caspian Basin (SCB). Despite the kinematic significance of the MKDF, previous geodetic measurements of the slip-rate across the fault have been highly variable, with a recent geological slip-rate supporting evidence for rapid motion across the fault. To resolve this ambiguity, we derive Sentinel-1 InSAR time-series in both the ascending and descending LOS (line-of-sight) to measure interseismic motion across the MKDF. This implements a processing strategy for the correction and performance analysis of tropospheric models from GACOS (Generic Atmospheric Correction Online Service), which suggests a 25–40 per cent underestimation in the amplitude of the tropospheric path delay in this region. Modelling the rate of fault-parallel motion across the MKDF and combining this with a geological slip-rate constrains 9 $\pm$ 2 mm yr$^{-1}$ right-lateral motion, along with a shallow locking depth of $\approx$6 km. The LOS time-series resolves path delays of greater than 1 mm yr$^{-1}$ in both LOS geometries to the north of the MKDF, aligned with mapped frontal thrust scarps to the north of the MKDF. Modelling this as uplift from deformation across these frontal thrusts estimates 4 $\pm$ 2 mm yr$^{-1}$ of shortening across the fault system. This implies that convergence measured with GNSS within the East Caspian Lowlands is partitioned across frontal thrusts to the north of the MKDF. Revising an Iran–Eurasia–SCB velocity triangle suggests that motion along the conjugate MKDF and Shahroud fault zones is representative of the motion of the SCB, which is moving at 10 $\pm$ 2 mm yr$^{-1}$ in a direction of 330° $\pm$ 10° relative to Eurasia.

**Key words:** Radar interferometry; Satellite geodesy; Seismic cycle; Asia; Time-series analysis; Continental tectonics: strike-slip and transform; Dynamics and mechanics of faulting.

## 1 INTRODUCTION

The Main Köpetdag Fault (MKDF) is a predominantly right-lateral, strike-slip fault that dissects the northern edge of the Köpetdag mountains of Turkmenistan and Iran (Fig. 1). The Köpetdag represent the northernmost expression of deformation within the Arabia–Eurasia collision east of the Caspian Sea, separating the Iranian Plateau, the broad zone of deformation which extends southwards for >2000 km from the Köpetdag and Alborz, from the Turan Platform, part of stable Eurasia to the north. The MKDF is recognized as an important element in regional tectonics as, together with the conjugate left-lateral Shahroud fault zone (SFZ), it facilitates the northwest motion of the South Caspian Basin (SCB), an aseismic block that moves independently to its surroundings (e.g. Jackson *et al.* 2002).

There are several major urban population centres in proximity to active structures surrounding the SCB. These include capital and major cities in Iran (Tehran, Mashhad), Azerbaijan (Baku) and Turkmenistan (Aşgabat), which have a combined population exceeding 15 million. Improving the characterization of seismic hazard posed by faults surrounding the basin therefore motivates understanding the motion of the SCB. However, constraining the precise rates, direction and poles of rotation of the SCB is difficult because there are no direct measurements from the basin interior due to water depths exceeding 1000 m and a thick sediment pile overlying the basement (>20 km; Jackson *et al.* (2002)). Determining the motion

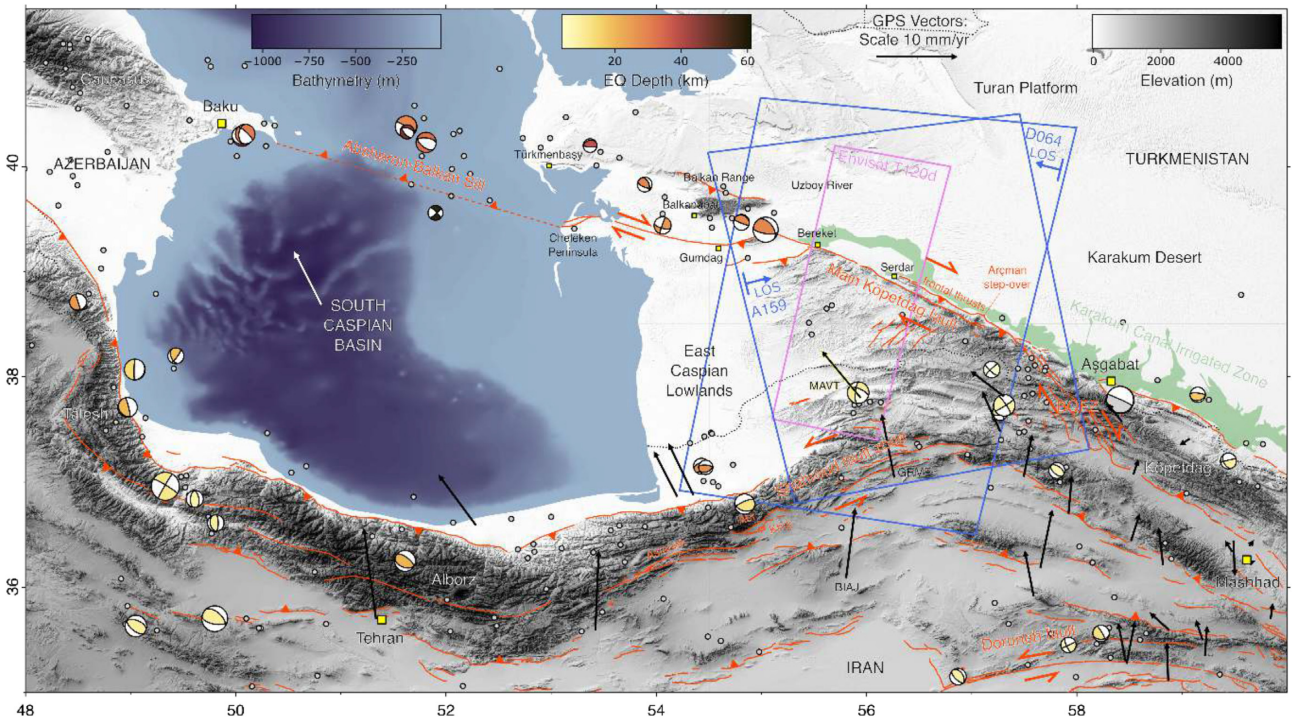


**Figure 1.** An overview of the active tectonics surrounding the South Caspian Basin. Active faults are delineated by red lines (Walker *et al.* 2021). The white vector represents the estimated motion of the SCB by Walker *et al.* (2021) (10.4 ± 1.1 mm yr$^{-1}$, 333° ± 5°). Earthquake focal mechanisms and depths are from the Global Waveform Catalogue (Wimpenny 2020), also with the 1948 M 7.3 Aşgabat (McKenzie 1972). Additional earthquake locations (grey circles) are from ISC-GEM (1906–1975; International Seismological Centre (2022), ISC-GEM Earthquake Catalogue; Storchak et al. 2013) and GCMT (1976–2020; Ekström et al. 2012). GPS vectors (black arrows) in NE Iran are from Mousavi *et al.* (2013) (MAVT highlighted in yellow). Sentinel-1 InSAR coverage from tracks D064 and A169 is outlined (blue), along with the Envisat track from Walters *et al.* (2013) (pink). The Karakum Canal irrigated zone is the green shaded region. South Caspian bathymetry is from the General Bathymetric Chart of the Oceans [GEBCO; Weatherall *et al.* (2015)]. Background is SRTM elevation-hillshade.

of the SCB instead relies on projecting measurements from along the boundaries of the block (i.e. the MKDF-SFZ conjugate system).

The northward GNSS velocity of northeast Iran relative to Eurasia decreases eastward from 11 mm yr$^{-1}$ at Tehran (52°E) to 1.5 mm yr$^{-1}$ at Mashhad (60°E, e.g. Khorrami *et al.* 2019). The velocity of GNSS stations along the southern shoreline of the Caspian Sea suggests that the motion of the SCB is to the northwest, either by lateral extrusion (Hollingsworth *et al.* 2008), or rigid body rotation around an Euler pole located in the Turan Platform (Djamour *et al.* 2010; Mousavi *et al.* 2013). GNSS-derived block models (e.g. Masson *et al.* 2007; Hollingsworth *et al.* 2008; Djamour *et al.* 2010; Mousavi *et al.* 2013) typically yield relatively low right-lateral slip-rates along the MKDF (3 ± 2 mm yr$^{-1}$; previous slip-rate estimates along the MKDF are summarized in Table S1). However Mousavi *et al.* (2013) acknowledges that these block models are unable to fit the velocity from the only GNSS station located within the interior of the onshore extent of the SCB in the East Caspian Lowlands (MAVT, Fig. 1). We note that this block model (Mousavi *et al.* 2013) neglects intrablock strain, which might be an important consideration as MAVT is possibly in the midst of a deforming mountain range.

Projecting the velocity of GNSS station MAVT onto the MKDF estimates a much higher rate of fault-parallel motion of 6.7 ± 0.5 mm yr$^{-1}$ on the MKDF, accompanied by 3.4 ± 1.0 mm yr$^{-1}$ of fault-perpendicular shortening (Mousavi *et al.* 2013). Such a higher slip-rate along the MKDF is supported by the late Quaternary geological slip-rate measurement of 9.1 ± 1.3 mm yr$^{-1}$ (Walker *et al.* 2021), from IRSL-dating of the abandonment of a displaced alluvial fan system (accompanied by 0.3 mm yr$^{-1}$ of shortening along frontal thrusts to the north of the MKDF). This is supported by the only direct geodetic slip-rate measurement across the MKDF of 8.5 ± 3.5 mm yr$^{-1}$ (Walters *et al.* 2013), derived from a single descending-track Envisat-InSAR time-series. In comparison, the rate of motion across the conjugate SFZ measured with InSAR (4.8 ± 0.8 mm yr$^{-1}$; Mousavi *et al.* 2015), GNSS (5.3 ± 1.3 mm yr$^{-1}$; Mousavi *et al.* 2013) and Quaternary dating (5.5 ± 1.5 mm yr$^{-1}$ summed across the Abr and Khuj segments; Javidfakhr *et al.* 2011) is relatively consistent.

Despite its apparent rapid slip-rate, there are no instrumentally or historically recorded earthquakes within the last few thousand years along the 200 km right-lateral strike-slip segment of the MKDF (from Bereket to the intersection with the BQFZ; Ambraseys & Melville 2005). Therefore very little is known about the capability of the MKDF to generate large earthquakes. The potential seismic hazard posed by the MKDF is exacerbated by the fault running directly parallel to the irrigated zone along the Karakum Canal (striking ≈135°), along which most of Turkmenistan's population is concentrated. Furthermore the apparent seismic quiescence along the MKDF is in stark contrast to adjacent regions (Fig. 1).

Directly to the east, the devastating 1948 $M_W$ 7.3 Aşgabat earthquake destroyed the capital city and killed an estimated 10 000–176 000 people (e.g. Tchalenko & Skempton 1975; Trifonov 1978). The Bäherden-Quchan Fault Zone (BQFZ), a distributed network of NNW–SSE striking faults at which the MKDF-SFZ conjugate converges in the eastern Köpetdag (e.g. Jackson *et al.* 2002; Shabanian *et al.* 2009b), has hosted the highest magnitude earthquakes recorded in the Köpetdag interior. These include the five-event

1851–1895 Quchan sequence, the 1929 $M_S \approx 7.0$ Baghan and 1997 $M_W$ 6.4 Bojnurd earthquakes (e.g. Hollingsworth *et al.* 2006; Shabanian *et al.* 2009a). In the eastern Alborz, the Astaneh segment of the SFZ is proposed to have hosted the highest magnitude event in the Arabia–Eurasia collision, the $M_S$ 7.9 865 A.D. Qumis/Damghan earthquake (Ambraseys & Melville 2005; Hollingsworth *et al.* 2010) (although the magnitude of this remains debated; Berberian & Yeats 2001). To the west, in the Balkan region between the Cheleken peninsula and Uzboy delta [assumed to represent the kinematic linkage to the active subduction along the Absheron-Balkan Sill offshore (e.g. Van Dijk *et al.* 2019; Jackson *et al.* 2002)], major recorded events include the 1895 $M_S$ 7.5 Krasnovodsk (present Türkmenbaşy) and 1946 $M_S$ 7.0 Balkanabat earthquakes.

Resolving the ambiguity in the rate of strain accumulation along the MKDF is required to characterize the hazard posed by the MKDF. InSAR time-series approaches have been used extensively to measure long wavelength and millimetres per year signals from interseismic motion across faults around the world (e.g. Weiss *et al.* 2020; Xu *et al.* 2021). This paper derives descending and ascending Sentinel-1 InSAR time-series to resolve surface deformation from interseismic motion along the MKDF. This aims to improve on the Envisat InSAR-derived measurement by Walters *et al.* (2013), which is derived from a single stack of 13 descending-track interferograms. Time-series measurements with Sentinel-1 are greatly improved compared to previous generations of satellites (e.g. Envisat). Acquisitions have a higher temporal frequency (6–12 d, it is possible to construct orders of magnitudes more interferograms), increased swath width (>250 km in range), higher spatial sampling (pixel size 2.5 m (cross-track) × 13 m (along-track) for Terrain Observation with Progressive Scans (TOPS), prior to multilooking), and more stringent satellite orbital control.

The location of the MKDF presents optimal conditions for maintaining spatial and temporal coherence within InSAR time-series, due to the high aridity, relatively muted topography (<1500 m), and limited sources of anthropogenic surface deformation (aside from along the Karakum Canal). The previous InSAR study of the MKDF (Walters *et al.* 2013) noted difficulty with high-magnitude tropospheric delays from water vapour content associated with the Caspian Sea (observed with the Medium-Resolution Imaging Spectrometer (MERIS) instrument aboard Envisat). Phase propagation delays through the troposphere are the primary limiting factor when deriving measurements of interseismic motion with InSAR (Doin *et al.* 2009), as these introduce high magnitude and long wavelength path delays to the differential radar phase. However empirical (e.g. Béjar-Pizarro *et al.* 2013; Bekaert *et al.* 2015; Tymofyeyeva & Fialko 2015) and global weather model corrections (e.g. Doin *et al.* 2009; Jolivet *et al.* 2011; Yu *et al.* 2017; Daout *et al.* 2018) aim to mitigate the effects of tropospheric path delays and improve the signal-to-noise ratio of tectonic signals in InSAR time-series. By exploiting the high temporal density of Sentinel-1 acquisitions, this study employs a novel approach to simultaneously implement and analyse the performance of tropospheric correction models.

## 2 SENTINEL-1 InSAR TIME-SERIES

### 2.1 InSAR time-series processing

We process Synthetic Aperture Radar (SAR) data from the ESA Sentinel-1 data archive using the New Small Baseline Subset (NSBAS; Doin *et al.* 2011, 2015; Grandin 2015; Grandin *et al.* 2016) processing chain [based on the ROI_PAC software; Rosen *et al.* (2004)]. Data from a single descending (D064) and ascending (A159) track covering the MKDF (>300 km in the azimuth/along-track direction, Fig. 1) are processed in interferometric wide-swath (IW) mode (swath width is ≈250 km in range/across-track).

The interferogram (IFG) networks span October 2014, to November 2019, and we construct 392 and 290 IFGs, from 126 and 96 acquisitions, for the ascending and descending track, respectively, with temporal baselines ranging from 12 d to over 1 yr. The interferometric networks are constructed semi-automatically; these initially include all possible date pairs within the same season (i.e. less than 3 months), additional pairs separated by 6 months and a year for each epoch, and manual additions to add connectivity and reduce redundancy for some dates. IFGs are constructed with 40 looks in range and 8 looks in the azimuth direction, giving a 160 m × 120 m effective horizontal spatial sampling. The range of perpendicular baselines is very low, with a maximum of ≈200 m. Both tracks have acquisition gaps of approximately 1 yr (ascending: 03/2017–03/2018; descending: 12/2014–10/2015). Multiple coherent IFGs are constructed over the acquisition gaps allowing the network to be continuous over the entire 5-yr period (IFG networks shown in Figs S1 and S2).

Unwrapping is relatively simple due to high InSAR phase coherence across the region, even within the Karakum Canal irrigated zone (KCIZ). Individual IFGs are unwrapped using a specific routine within the NSBAS processing chain, which allows us to keep both high and low frequency constraints, following Grandin *et al.* (2012). The unwrapping steps are as follows: (1) we replace the amplitude of the IFGs by the phase colinearity as defined by Pinel-Puysségur *et al.* (2012), in order to reduce sensitivity to pixels with strong backscatter; (2) we use a filter that is an average of the complex phase, in triangular sliding windows, by the spatial colinearity previously computed (Doin *et al.* 2011); (3) following this, we impose an unwrapping path that goes from high to low coherence areas as defined by the filter averaging process on complex values (Grandin *et al.* 2012). (4) Afterwards we compute the phase difference between the unwrapped phase and a set of less-filtered IFGs obtained with the Goldstein-Werner filter (Goldstein & Werner 1998). The residual is assumed to be between $-\pi$ to $\pi$, and is added back to the unwrapped phase (López-Quiroz *et al.* 2009; Chen *et al.* 2015). This procedure is essential for long-baseline IFGs as the sliding window filter allows successful unwrapping over wide areas while the high-frequency signal is added back to the smooth unwrapped phase.

### 2.2 Implementation of tropospheric phase-delay corrections

Phase propagation delays through the troposphere are often divided into a stratified component, which correlates with the topography and a turbulent component (Hanssen 2001; Doin *et al.* 2009; Jolivet *et al.* 2011). To mitigate the effect of tropospheric signals, we use tropospheric phase-delay corrections derived from HRES-ECMWF atmospheric models supplied by GACOS [Generic Atmospheric Correction Online Service; Yu *et al.* (2017, 2018b, a)]. GACOS utilizes an iterative tropospheric decomposition model to separate the stratified and turbulent components of the atmospheric model signal, integrating continuous GNSS tropospheric delay estimates. GACOS tropospheric corrections are applied to unwrapped IFGs prior to time-series inversion, using an approach that simultaneously computes a statistical analysis of their performance.

Prior to implementing an atmospheric model-derived tropospheric model, we explored the use of empirical corrections in the time-series inversion. Corrections using estimations of phase-elevation relationships were unsuccessful due to the variability of the relationship in space. In addition we observe that they remove part of the deformation signal (Fig. S3). These are difficult to capture with a relatively simple relationship (linear) and muted topography, in comparison to previous studies in more mountainous regions (e.g. Elliott *et al.* 2008; Béjar-Pizarro *et al.* 2013; Bekaert *et al.* 2015; Tymofyeyeva & Fialko 2015)). Another possibility is that the sources of tropospheric path delay may vary across a large region and a single fit may not yield a good match (e.g. Murray *et al.* 2019; Shen *et al.* 2019). Increasing the complexity of this relationship might trade-off even more than a simple linear phase–elevation relationship with deformation because the expected gradient of surface displacement from right-lateral strike-slip motion is colocated with higher topography to the south (as we expect a non-linear deformation signal).

Time-series velocity maps can be biased due to aliasing of oddly sampled time-varying atmospheric signals (e.g. Doin *et al.* 2009; Daout *et al.* 2018). The stratified tropospheric phase delay, which correlates with topography, has smooth changes in time and is dominated by a seasonal term with an amplitude depending on the variation of temperature, pressure and humidity in space and time (Doin *et al.* 2009). Due to the temporal sampling of Sentinel-1, we also explore the effect of decomposing the time-series into a seasonal function to capture this tropospheric signal. However we observe poor results due to large outliers from this seasonal behaviour (Fig. S4). These abrupt changes are possibly due to water vapour from weather systems moving around the Caspian Sea observed by Walters *et al.* (2013), which result in turbulent tropospheric path delays and bias the linear trend in the velocity estimation.

The tropospheric correction strategy using the GACOS models follows a sequence of steps (Fig. 2): (1) for each unwrapped IFG, we calculate a tropospheric phase-delay map in radar slant geometry from the GACOS models (supplied as a zenith path delay per date). (2) We solve for a linear ramp and offset in range and azimuth between the unwrapped IFG and tropospheric phase-delay; over a swath-scale distance this is unlikely to remove any deformation signals which are non-linear. The residual ramp may reflect residual long-wavelength signals, such as ionospheric, turbulent tropospheric, orbital or plate motion drifts that have not been accounted for. (3) To ensure phase closure is maintained over the IFG network, we invert the ramp parameters individually for each epoch in the time-series assuming no covariance between the parameters. (4) For each IFG, we reconstruct the tropospheric phase-delay using the inverted ramp parameters. (5) We then apply the correction by subtracting tropospheric phase-delay from the individual IFGs, with both the data and model referenced to a 50 × 50 pixel area, using the mean of the phase weighted by the colinearity, assumed to be a stable non-deforming zone (away from known active structures, high topographic gradients, anthropogenic deformation sources and basin interiors; Maubant *et al.* 2020).

### 2.3 Ensemble performance metrics of tropospheric models

Determining the performance of tropospheric phase-delay corrections is difficult due to differences in the spatial and temporal scales of interest, and variability in reliability depending on the region to which they are applied (Murray *et al.* 2019). Assessing the spatial performance typically involves determining the reduction in the variance or noise characteristics, and residual empirical relationships in the data. Temporal performance metrics quantify the variance of individual pixels through time relative to the inverted functional form of the time-series.

We compute three metrics to assess the performance of the GACOS corrections over the entire time-series network. This makes use of the assumption that for a network of short baseline IFGs, most of the signal in each IFG is from atmospheric path delays. If an atmospheric correction model is performing well, it should capture the majority of phase variation in the IFG. The metrics are determined for individual IFGs, before being compiled into a histogram to analyse the ensemble performance of the corrections over the network of IFGs (examples of the correction strategy on individual IFGs are provided in Figs S5–S7). These performance metrics are then integrated as weightings into the subsequent time-series analysis.

The first metric estimates the gradient of the interferometric phase delay, subtracting the reconstructed linear ramp phase, versus the phase due to atmospheric path delay (i.e. the ratio of the two phase delay estimates). This measures the performance of the amplitude of the atmospheric correction. If the correction is performing perfectly, there should be a linear trend in the phase-phase plot with a gradient ≈1. The second metric calculates the Pearson correlation coefficient ($-1 \leq r \geq 1$) between the IFG phase and the atmospheric correction phase. This measures the spatial performance of the correction, which if the correction is performing well will return a positive linear correlation with $r \approx 1$. The third metric computes the change in variance between the initial interferogram and the corrected interferogram. Good performance of the correction will result in a significant reduction in the variance, as both topographically correlated and turbulent tropospheric signals are accounted for. By calculating the reduction in standard deviation, we account for pairs where the observed phase and model correction phase variation is small. In these cases the gradient and correlation metrics might suggest poor performance as other sources of noise account for most of the signal.

For both the descending and ascending tracks, the performance metrics are consistent (Fig. 3). The histogram of the gradients for the time-series are normally distributed with modal values of 0.70 ± 0.19 (D064) and 0.61 ± 0.19 (A159). Very few model-data pairs have a gradient ≥1 (i.e. over correction of the phase by the atmospheric model), negative (i.e. reverse sign of the atmospheric model), or close to zero. The correlation metrics have a negative skew with modal values of 0.81 ± 0.14 (D064) and 0.75 ± 0.14 (A159). Combining the gradient and correlation metrics suggests the atmospheric correction models are performing excellently spatially, although the amplitude scaling suggests there might be a swath-scale underestimation of the amplitude of the model correction in this region. The modal reduction in standard deviation of the interferograms after correction is ≈25 per cent for both networks. The model-data pairs with a low gradient generally have a low correlation and poor standard deviation reduction, with several of these cases increasing the standard deviation after correction (Fig. 3).

### 2.4 Time-series inversion

Time-series of displacements in the line-of-sight (LOS) are reconstructed using the NSBAS method (Doin *et al.* 2015). The phase delays of unwrapped IFGs are inverted pixel by pixel, to solve for the incremental phase delay of each date relative to the preceding date in the time-series. The total phase delay is then obtained by

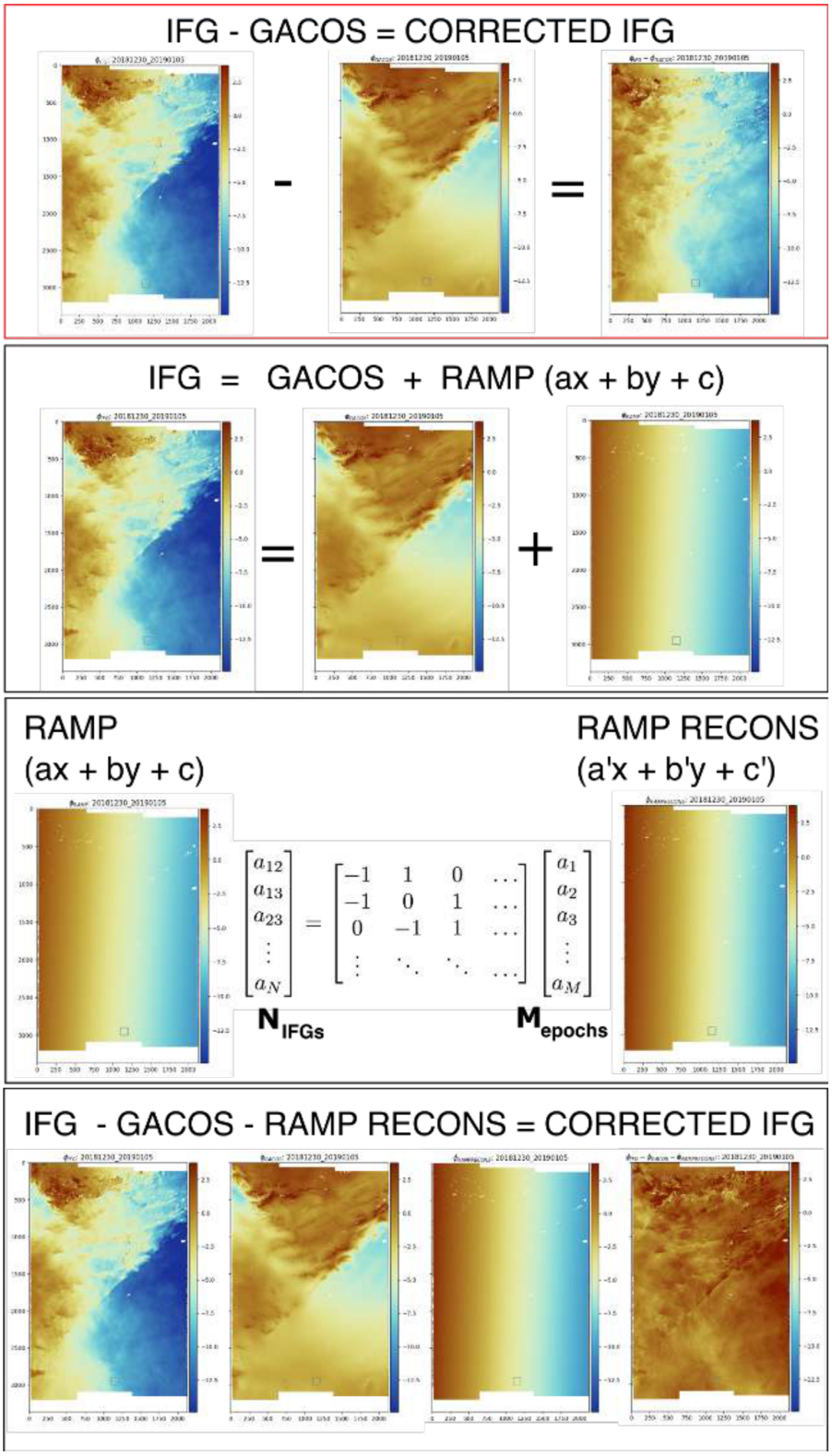


**Figure 2.** Processing strategy for applying tropospheric path-delay corrections, applied to individual interferograms (example from ascending track A159). From top to bottom: applying the GACOS correction directly results in a high amplitude residual signal in the corrected phase (red outlined box). Instead we solve for a linear ramp between the IFG and the GACOS correction. Next we invert the interferometric ramp parameters for ramp parameters at each epoch, re-estimating the interferometric ramp parameters from these in order to ensure phase closure in the time-series. Finally we apply the correction using *IFG − GACOS − RAMPRECONS*. and reference each corrected IFG to a stable undeforming region. Comparing the final phase maps on the top and bottom panels are representative of the corrections over the entire network, applied prior to time-series inversion.

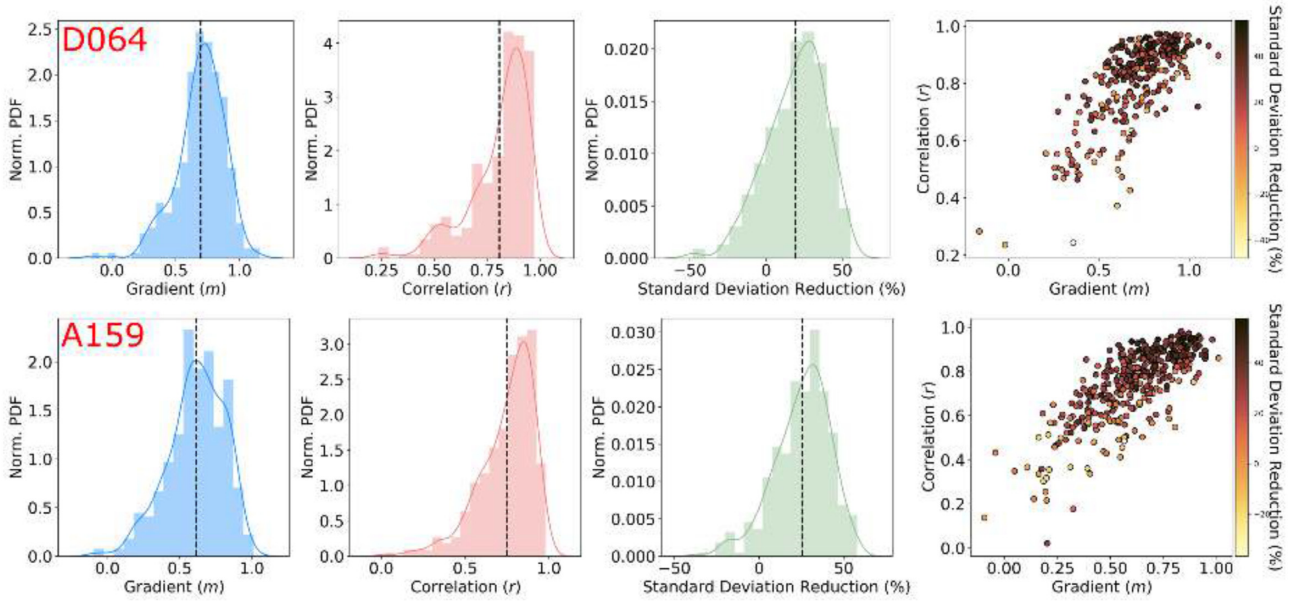


**Figure 3.** Performance analysis of the tropospheric path-delay model corrections on the interferometric phase. Descending track results are along the top row, with ascending track results along the bottom row. From left- to right-hand panels: the gradient of the interferometric phase versus the tropospheric path-delay; the correlation coefficient between the observation and the model; the reduction in the standard deviation from correcting the interferogram with this method (normalized percentage); scatter plot showing the relationship between the metrics (gradient versus correlation, coloured by the standard deviation reduction). Dashed grey lines show the mean value for each metric.

adding incremental phase delays, relative to the first date in the time-series which is set to zero. The system of equations is solved using least squares with regularization provided by additional constraints (López-Quiroz *et al.* 2009). The regularization allows for adjustment of disjoint portions of the time-series network where the inversion is underdetermined. However, given the frequent temporal sampling of the network and high proportion of unwrapped pixels, only a few pixels are affected in each epoch and a low smoothing coefficient is applied (0.003).

During the initial time-series inversion, we map inconsistencies in the interferometric network using the root-mean-square (RMS) misclosure of individual pixels in the time-series (López-Quiroz *et al.* 2009). This is used to semi-automatically detect unwrapping errors which result in high RMS-misclosure, with problematic interferograms either re-unwrapped or discarded if the network remains connected. Iterations of the time-series inversion are repeated until no large network inconsistencies remain. In a final step, we improve the reference frame selection and the time-series decomposition using an iterative procedure to extract an average velocity from a linear fit to the time-series of the form $\phi_k = V \times t_k$, where $\phi_k$ is the phase change of a pixel over the cumulative time $t_k$ from the first epoch (e.g. Daout *et al.* 2018). At each iteration, the reference is re-estimated in non-deforming areas, and the misfit between the reconstructed phase delays and the linear evolution is used as weighting in the next iteration.

The resulting products are rate-maps of the average surface LOS velocities in mm yr$^{-1}$ (Fig. 4). Uncertainty maps are also computed, equal to the RMS of the misfit of the cumulative displacements in the time-series to the linear time variance of the model (Fig. S8). Prior to plotting, the time-series velocity maps are masked using the final evaluation of the RMS-misclosure for each pixel using a masking threshold of 2.5 mm.

## 3 RESULTS

### 3.1 InSAR LOS velocity fields

The primary feature of surface deformation in both LOS velocity fields is a long wavelength signal from right-lateral motion across the MKDF (Fig. 4). In the descending LOS, there is a ≈3–4 mm yr$^{-1}$ velocity gradient from blue to the south of the fault, to red/orange to the north of the fault. Similarly in the ascending LOS, the velocity gradient has the opposite sign reflecting the right-lateral motion observed from a different LOS. The magnitude of the velocity step across the fault is greater in the descending LOS, as expected due to the optimal orientation of the descending LOS vector to resolve any fault-parallel (strike-slip) component of motion.

In both the ascending and descending LOS, a 10–30 km wide zone adjacent to the north of the MKDF has a positive signal (≈1–2 mm yr$^{-1}$ relative to the Turan platform). This implies a broad zone of decreased phase delay, almost identical in both LOS geometries, in the 'badlands' that separate the MKDF and Karakum Canal irrigated zones. The signal does not correlate with topography which here is generally gently sloping to the north (versus to the south where the ridges of the Köpetdag mountains lie). The northern extent of this signal is masked by a very high-magnitude (an order of magnitude greater) and short-wavelength deformation signal along the Karakum Canal irrigated zone. Assuming the signal is tectonic in origin, it is consistent with uplift from motion across mapped frontal thrusts to the north of the MKDF (Hollingsworth *et al.* 2008; Walker *et al.* 2021). Shortening across frontal thrusts will result in vertical and fault perpendicular motion which will both be resolved by the ascending LOS vector. In contrast the descending LOS vector will only resolve vertical motion as it is insensitive to fault-perpendicular motion (Fig. S9). Decomposing the

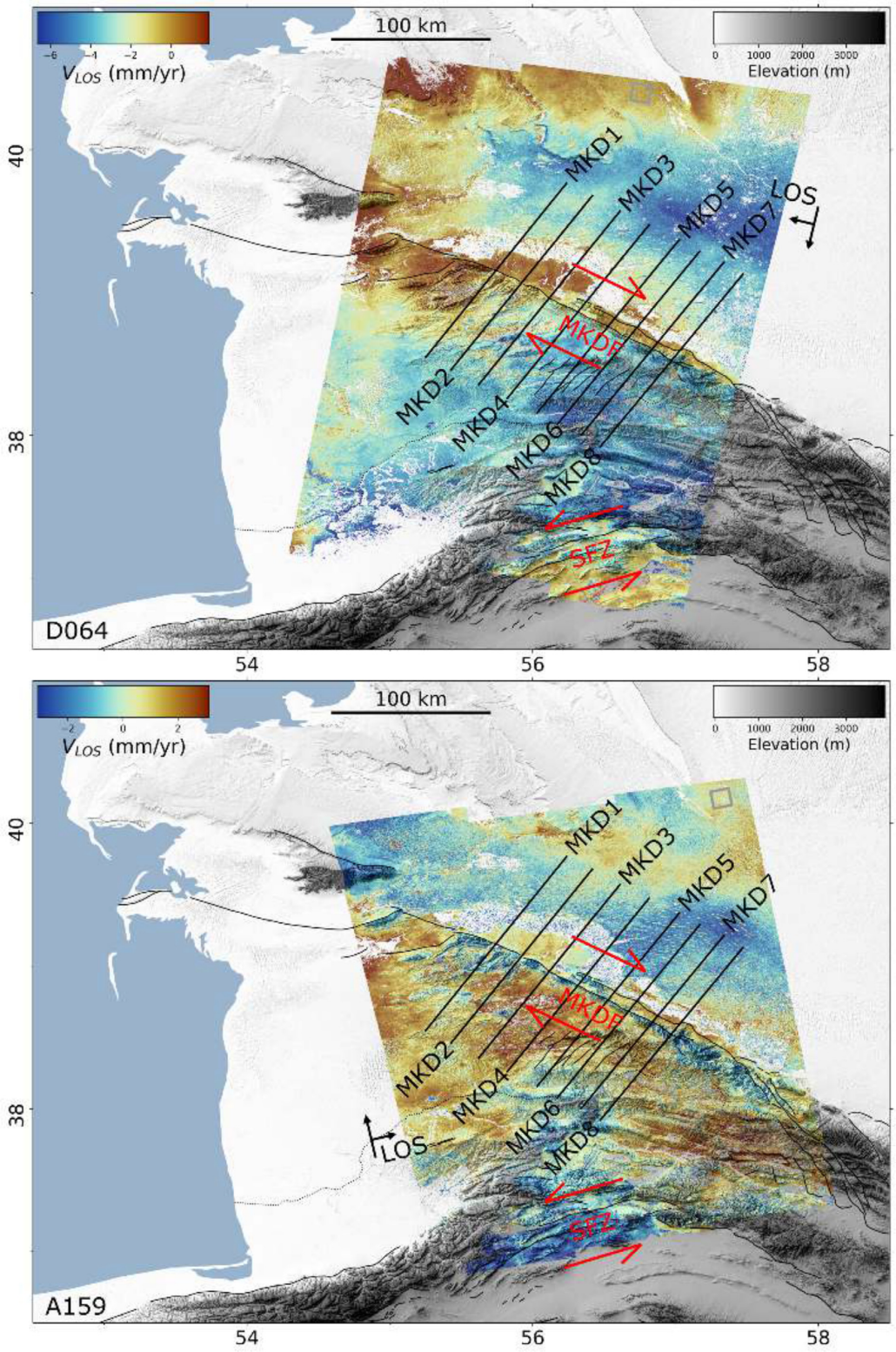


**Figure 4.** LOS velocity maps from the time-series analysis for D064 (top panel) and A159 (bottom panel). Active faults are delineated by black lines (Walker *et al.* 2021), with the MKDF and SFZ labelled in red. Profile locations MKD1–8 (from west to east) are shown by bold the black lines, perpendicular to the strike of the MKDF. Swaths are 20 km wide and 160 km long, centred on the mapped fault trace, containing the data projected onto each profile. Red is surface motion towards the satellite LOS, blue is surface motion away from the satellite LOS, with both LOS velocity fields spatially referenced to near the far north of the image (grey rectangles).

LOS velocity fields into fault-parallel and vertical components also demonstrates the spatial characteristics of the inferred uplift signal (Fig. S13).

There are multiple non-tectonic signals in the LOS velocity fields. There are low-magnitude ($\approx$1 mm yr$^{-1}$, consistent sign in ascending and descending) topographically correlated residual signals, most notably delineating valleys in the high Köpetdag to the southeast and along the northern most Köpetdag ridge in the ascending velocity field. There are additional surface hydrological deformation sources with high-magnitudes and short-wavelengths associated with agriculture in valleys, which we attribute to subsidence from water extraction. There is also uplift in marginal irrigated areas, such as extending away from the Karakum Canal in the arcuate deviation of the KCIZ between Bereket and Serdar. Another observation is the uplift of takyrs ($\approx$1 mm yr$^{-1}$), natural clay basins, in the Karakum Desert; the pock-marked effect on the Turan Platform (Fig. 4). Again the very short wavelengths of these signals are indicative of near-surface deformation processes.

### 3.2 Fault-perpendicular LOS velocity profiles

To begin to investigate long-wavelength tectonic signals from interseismic motion along the MKDF, we plot fault-perpendicular profiles (Figs 5) of the LOS velocity at regularly spaced along-strike intervals from $\approx$55 to 57°E (locations MKD1–8 are from east to west; Fig. 4). Profiles are centred on the mapped surface trace of the MKDF, and are perpendicular to a strike of 123°. The profile swath has length 160 km and width 20 km, with a linear trend and offset removed from each profile (an obvious linear trend remains in several of these as we have not tied the arc-tangent-shaped deformation to a model or known reference at this point). The standard deviation of the LOS velocity in each profile, computed in sliding windows, is generally 1–2 mm yr$^{-1}$, apart from within the intersection of the Karakum Canal irrigated zone (Fig. 5).

The profiles demonstrate the expected long-wavelength signal from right-lateral motion along the MKDF (Fig. 5), with opposing sign step changes of 3–4 and 1–2 mm yr$^{-1}$ resolved in the descending and ascending LOS respectively. There is no obvious correlation at long wavelength with topography directly to the south of the MKDF. The wavelength of the tectonic signal is generally concentrated within $\leq$40 km either side of the fault. The wavelength of the signal appears to increase heading westward. As discussed above, in both the descending and ascending LOS there is a 10–30-km-wide zone of reduced path delay that we interpret as uplift adjacent to the north of the MKDF.

### 3.3 Investigating systematic biases in InSAR time-series

The influence of systematic biases in InSAR time-series using short temporal baselines has recently been raised by Ansari *et al.* (2020). This bias might arise from abrupt systematic decorrelation of the radar phase in distinct portions of asymmetrical surface deformation cycles growth (Daout *et al.* 2020), or non-linear filtering and averaging during processing (e.g. Ansari *et al.* 2020). This may subsequently result in velocity biases in time-series inversions. To mitigate potential biases, the interferometric networks for the ascending and descending tracks have a wide range of temporal baselines. Following the advice of Ansari *et al.* (2020) and Daout *et al.* (2020), we investigate the effect of removing short temporal baseline interferograms on the deformation retrieval with descending track D064 (Fig. S10).

Removing short temporal baseline IFGs ($\leq$12 d) has no effect on long-wavelength signals in the LOS rate-maps. There is a resolvable difference with a limited number of pixels constrained to zones of rapid subsidence, the majority of which are along the Karakum Canal. Most of these pixels are subsequently masked during our analysis as they typically have high RMS-misclosure. We also investigate changes to phase-elevation relationships when removing short baseline IFGs, to probe possible increases in biases associated with increased soil moisture effects in regions of higher topography. We do not observe changes to phase-elevation relationships with no discernible difference in the time-series velocity maps (Fig. S10). Having established no evidence for systematic biases in the descending time-series analysis, we retain a limited number of IFGs with temporal baselines of $\leq$12 d in the ascending time-series network as these contain useful information for detecting phase-misclosure in the time-series inversion procedure.

## 4 MODELLING

To model surface deformation from interseismic motion along the MKDF, we use Flower2D (Daout *et al.* 2016a, b); a geodetic tool package for the 2-D exploration of fault geometry and slip-rates within a Bayesian framework. For each model, we run 100 000 synthetic surface displacement models with the PyMC Monte Carlo Markov Chain (MCMC) algorithm (not using a back-slip approach). The results present the posterior distribution of parameters, having discarded the first 50 per cent of these models (burn-in period). Initially we model the resolved deformation as a dislocation on a vertical strike-slip fault in a 2-D elastic half-space, before progressively increasing and justifying structural complexity from geodetic and geological observations.

Combining the descending and ascending LOS, we observe two components of the 3-D surface deformation field. The ascending LOS is sensitive to all three potential components of motion along the MKDF: fault parallel, fault perpendicular and vertical. In contrast, the descending LOS vector is almost parallel to the strike of the MKDF is therefore insensitive to fault-perpendicular motion (shortening), whilst also being optimally oriented to resolve fault-parallel motion (strike-slip). To provide a comparison to the geological slip-rate from Walker *et al.* (2021), we select profiles that are approximately colocated to their sampling region (profiles MKD5–7). This avoids the western and eastern limits of the MKDF (profiles MKD1 and 8), and also the widest section of the Karakum Canal irrigated zone (intersecting profiles MKD2–4). The swath widths are the same as those presented in Fig. 5. We remove outliers ($2\sigma$-percentiles) from the data around a 1 km sliding-median window, and tie the deformation in each profile to the model with a linear trend and offset. The linear trend removed in each model is very low ($<$0.001 mm yr$^{-1}$ km$^{-1}$) which is unlikely to remove any deformation signals within the noise levels of the data ($\approx$1 mm yr$^{-1}$), and instead applies minor rotational adjustments to tie the LOS data to the model.

The LOS velocity fields are projected into UTM coordinates (WGS 84/UTM zone 40N) and downsampled to 250 m using a bi-cubic interpolation (as are their related uncertainties, Fig. S8). The downsampling corresponds to the length-scale on which the covariance of the LOS velocity decays with distance, using the empirical approach of Sudhaus & Jónsson (2009) (Fig. S11). The variation in incidence angle of Sentinel-1 IW mode (29.1–46.0°) is also accounted for.

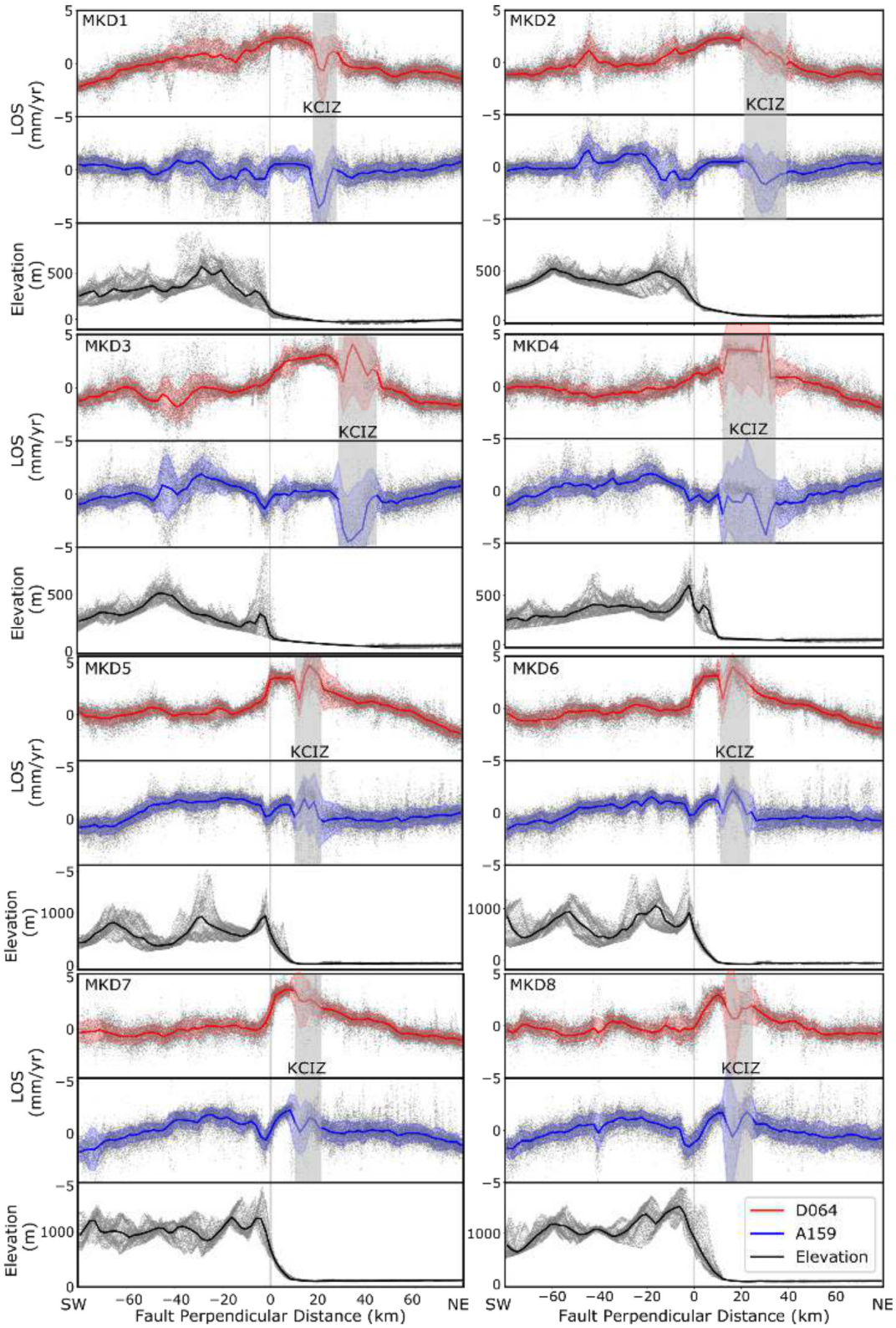


**Figure 5.** Profiles MKD1–8 (west to east, locations in Fig. 4). Profiles are centred on the mapped trace of the MKDF (vertical grey dashed line). Descending D064 (red) and ascending A159 (blue) profiles have a linear trend and offset removed. The bold line shows the sliding median, with the shaded region the standard deviation within the window. Topography is shown in the lower panel of each figure in black. The Karakum Canal irrigated zone (KCIZ) is shaded in light grey, characterized by low point density and high standard deviation.

### 4.1 Initial strike-slip model

Assuming interseismic motion along the MKDF is purely right-lateral strike-slip (e.g. Walters *et al.* 2013; Walker *et al.* 2021), the descending LOS is optimally oriented to resolve horizontal fault-parallel motion. Therefore we initially model the deformation resolved only in the descending LOS. We model interseismic deformation as a buried vertically dipping infinite screw dislocation in a 2-D elastic half-space (Savage & Burford 1973), which has a constant right-lateral slip-rate, *SS*, below a locking depth, *H*. For each parameter we assign a uniform prior distribution. For the slip-rate, the distribution encompasses all previous slip-rate estimates along the MKDF ($8 \pm 5$ mm yr$^{-1}$). The location of the MKDF is fixed to the mapped surface trace, and the locking-depth prior is $30 \pm 30$ km (uniform prior distribution).

The results of the initial model suggests that right-lateral motion across the MKDF is 6–7 mm yr$^{-1}$ (Figs 6a, S14a and S15a). However the simple model geometry is unable to fit near-fault signals (within 30–40 km), which we infer result from structural complexity along the MKDF. Therefore we neglect the posterior distribution of the locking depths. The estimated rate of motion will likely be overestimated as vertical deformation to the north of the fault will sum constructively with right-lateral signals when resolved in the descending LOS (e.g. Walters *et al.* 2013). We repeat these models using different profile lengths and observe that the slip-rate changes with the length of the profile (Fig. S12). When profiles are $\leq$120 km the rate of motion systematically increases, due to the overfitting of the uplift signal to the north of the MKDF. Similarly in profiles exceeding 160 km in length, the slip-rate also systematically increases. This is possibly due to the profiles intersecting long wavelength signals away from the MKDF that we have not accounted for. Therefore in subsequent models we restrict the profile lengths to 120–160 km.

Next we proceed to jointly invert for deformation resolved in the ascending LOS into our initial model (Figs 6b, S14b and S15b). The inclusion of the ascending LOS reduces the fault parallel slip-rate, with the rate of fault-parallel motion decreasing to $6.1 \pm 0.3$ mm yr$^{-1}$. The inclusion of the ascending LOS confirms our suggestion that the signal adjacent to the north of the MKDF might result from a combination of vertical and fault-perpendicular motion. We propose this signal results from motion across mapped frontal thrust faults described in Walker *et al.* (2021), which requires modelling the MKDF with a more structurally complex fault geometry.

### 4.2 Strain-partitioning geometry

Making the assumption that the near-field deformation to the north of the MKDF is from motion across frontal thrusts, we model deformation resolved in the descending and ascending LOS with a strain-partitioning geometry. The model geometry consists of a semi-infinite horizontal elastic dislocation, at a depth $H_B$ (uniform prior; $30 \pm 30$ km), which aims to model the convergence accommodated by a décollement or a shear zone. Branching off from this primary structure is a vertical strike-slip fault, with horizontal position fixed to the mapped surface trace of the MKDF and locked up to a depth $H_A$ (uniform prior; $30 \pm 30$ km). An additional structure branches off at the same point (i.e. a frontal thrust), which propagates to the north (positive horizontal distance) up to a locking depth $H_{TH}$ (uniform prior; $30 \pm 30$ km). The additional structural parameter is the horizontal distance of the thrust fault tip from the strike-slip fault, $D_{TH}$ (uniform prior; $30 \pm 30$ km).

We impose pure strain-partitioning in which the convergence across the fault system, corresponding to the horizontal block motion with both strike-slip and dip-slip motion ('Conv.' = 'SS' + 'Short'), is partitioned into a strike-slip ('SS') component on the vertical strike-slip fault (MKDF), and shortening ('Short') along the flat dislocation is projected to dip-slip motion on the frontal thrust. For the prior distribution of convergence rate accommodated by the horizontal dislocation, we centre a Gaussian distribution on the projected shortening from GNSS station MAVT onto the MKDF (3.5 mm yr$^{-1}$) with double the standard deviation (0–7.5 mm yr$^{-1}$, $2\sigma$ range). As multiple dip angles of the frontal thrust could agree with the surface displacement data, the projection of the shortening across the fault system into a unique dip-slip motion along the ramp, allows, with a long-term compatibility of the geometry, the reduction of the number of possible models in agreement with the data.

The pattern of uplift observed in both the ascending and descending LOS is fit by the structural configuration, and the rate of fault-parallel motion is consistent with the previous models (Figs 6c and S15c). The posterior distribution of the rate of convergence perpendicular to the fault system is $4 \pm 2$ mm yr$^{-1}$. The models suggest a relatively shallow locking depth of $6 \pm 2$ km for the strike-slip fault (MKDF). As discussed previously, the spatial extent of the uplift signal is difficult to constrain due to the overprinting by hydrological signals along the Karakum Canal. This likely obscures the true locking depth and propagation extent of the thrust faults. This is reflected in the broad posterior distributions of these parameters. The thrust fault propagation appears to be highly variable along strike ($\approx$10–30 km to the north of the MKDF), with a relatively shallow locking depth of 2–6 km. Similarly the horizontal dislocation depth is poorly constrained with a broad posterior distribution.

## 5 DISCUSSION

### 5.1 Tropospheric model corrections

The removal of tropospheric phase-delays in the time-series is demonstrated by the low levels of residual topographic correlation (Fig. 5) and high-amplitude turbulent signals in the LOS velocity fields (Fig. 4). However the tropospheric correction performance analysis suggests that, in this region, tropospheric models systematically underestimate the amplitude of the correction by 25–40 per cent (gradient metric). This contrasts with the spatial performance of the tropospheric models using the correlation metric, with values close to 1 implying that the corrections reproduce spatial patterns attributed to tropospheric signals in individual IFGs excellently. In part, this is relatively simple to explain; the spatial performance is inherently better due to the autocorrelation of the interferometric phase and the model tropospheric path delay with topography.

The systematic under-estimation of the scaling amplitude at a swath-width scale requires further investigation. We are hesitant to use methods that scale global weather model-derived tropospheric corrections at variable length scales here (e.g. Shen *et al.* 2019), due to possible trade-offs between deformation and tropospheric models. Instead amplitude underestimation could possibly be accounted for by other sources of long-wavelength signals that introduce variability in path delay, such as ionospheric signals. Alternatively global weather models might be missing regional scale water fluxes or incorrectly advecting water vapour, due to very few data observations in this remote region. We suggest implementing

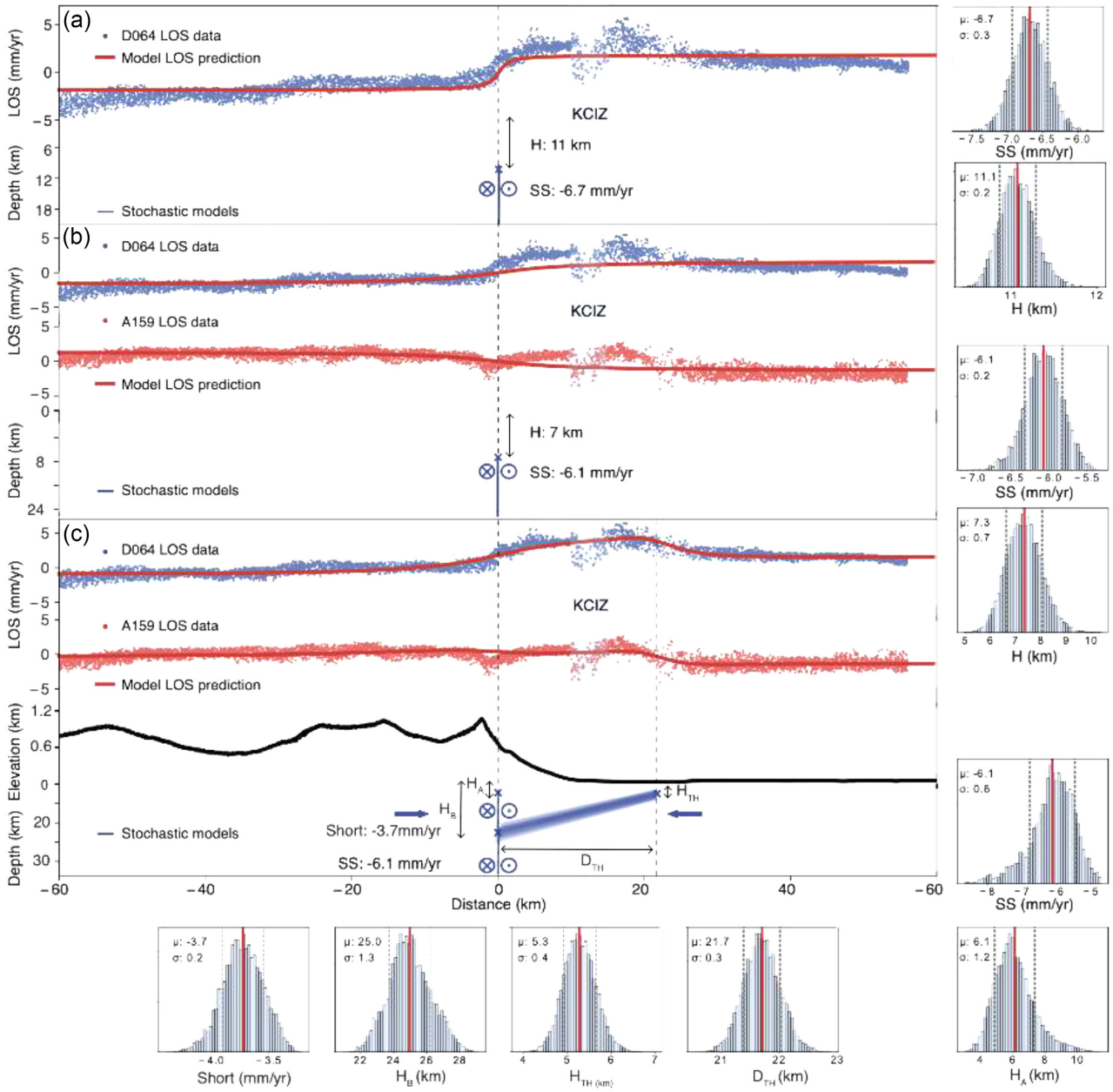


**Figure 6.** Modelling approach with profile MKD6 (120 km length, 20 km width). The results of the Bayesian exploration of parameters in each inversion are shown by the histograms on the right. (a) Modelling only the optimally oriented descending LOS with a vertical strike-slip fault. (b) Modelling both the descending and ascending LOS with the same vertical strike-slip geometry. (c) A more structurally complex model, with the introduction of a thrust fault to the north of the MKDF (location of the strike-slip fault fixed to the MKDF). The intersection of the Karakum Canal irrigated zone (KCIZ) is highlighted by the blue shading. The deformation is tied to each model with the removal of a linear ramp and offset.

the tropospheric correction performance analysis to other locations around the world with potential differences in the quality of weather models, to test whether better constrained regions have improved amplitude metric scaling relationships.

### 5.2 Deformation from hydrological sources

The most prominent non-tectonic deformation sources resolved in the LOS velocity fields are related to hydrological processes, predominantly throughout the irrigated zone along the Karakum Canal. The Karakum Canal diverts water across the Karakum desert, with a total length of >1400 km. The canal sources water from the Amu Darya River, the main downstream drainage system of the Pamir mountains far to the east along the border with Tajikistan and Afghanistan. The majority of Turkmenistan's 5.85 million population lives along, and is dependent on, this irrigated zone for agriculture and economically important exports. The thin strip of land, 5–25 km wide, is located at the distinct change in topographic gradient between the foothills of the Köpetdag and the low-relief expanse of the Karakum Desert to the north. Concerns have been raised regarding water mismanagement in such an arid region primarily dependent on distal sourcing (O'Hara 1997).

Our observations demonstrate the potential for the use of Sentinel-1 InSAR time-series to provide remote observations for

water management. The short wavelength signals along the KCIZ generally have a negative sign in both the ascending and descending LOS which implies subsidence, and have high-magnitude in comparison to tectonic signals. Subsidence is typically $>10$ mm yr$^{-1}$ resolved in the LOS and exceeds 50 mm yr$^{-1}$ in localized parts of the KCIZ (Fig. 7). Agricultural subsidence is commonly observed with InSAR and is typically attributed to groundwater extraction. However, in this region agricultural subsidence is surprising as we expected that most of the water is sourced directly from the Karakum Canal. This suggests that a high fraction of the agricultural water budget is supplemented by the local water table.

### 5.3 Interseismic motion and strain-partitioning

To combine the modelling results (profiles MKD5–7), we take the weighted mean of the posterior distributions. The weighted mean, accounting for the standard deviation ($\sigma$) of multiple measurements ($x_1, \ldots x_i$), is $\hat{\mu} = \frac{\sum \frac{x_i}{\sigma_i^2}}{\sum \frac{1}{\sigma_i^2}}$. To provide a conservative measure of the error we state the entire range of the posterior distribution standard deviations. This constrains the right-lateral slip-rate along the MKDF to $7.2 \pm 2.4$ mm yr$^{-1}$. Using the same method, we constrain the rate of shortening across the frontal thrusts to $4.3 \pm 1.5$ mm yr$^{-1}$.

The right-lateral slip-rate is comparable within error to the GNSS-derived estimate from Mousavi *et al.* (2013), the Envisat-InSAR derived geodetic measurement from Walters *et al.* (2013), and the geological slip-rate from Walker *et al.* (2021). In comparison to the descending LOS derived slip-rate from Walters *et al.* (2013), our measurement is benefited by the inclusion of the ascending LOS. Using a single LOS (e.g. Walters *et al.* 2013) with additive fault parallel and vertical signals on one side of a fault (from the proposed structural geometry) may overestimate slip-rates if modelling the pattern of deformation with a single vertical strike-slip fault. From the inversion of the surface deformation, the locking depth of the MKDF is ≈6 km, which we note is relatively shallow for a continental strike-slip fault (e.g. Vergne *et al.* 2001).

If uplift to the north of the MKDF results from inferred shortening across frontal thrust faults, there are implications from both a seismic hazard and regional tectonics perspective. The frontal thrusts run parallel to the KCIZ (e.g. Walker *et al.* 2021). The models suggest they might extend very close to or directly beneath this populated region. The InSAR observations are supported by geomorphological evidence with evidence for anticlinal folding to the north of the MKDF (Walker *et al.* 2021). The posterior distributions of model geometries estimates that the dip angle of the thrust faults ranges from 20° to 42°. With this geometry and shortening rate, we estimate the rate of uplift along the frontal thrusts is 1–5 mm yr$^{-1}$.

The rate of shortening is consistent with the motion of GNSS station MAVT. Mousavi *et al.* (2013) project this vector to estimate $3.5 \pm 1.0$ mm yr$^{-1}$ of fault-perpendicular shortening is accommodated between the SCB and the Turan Platform. This is either by internal block deformation in the East Caspian Lowlands (and extending into the western Köpetdag), or is transferred to the MKDF system. Another consideration is reconciling the rate of uplift with the 0.3 mm yr$^{-1}$ of shortening along frontal thrust scarps (Walker *et al.* 2021), derived from IRSL-dating of an alluvial fan surface displaced by the thrust scarp. Walker *et al.* (2021) states that this measurement represents a minimum estimated value for the rate of shortening. Our models suggest that the frontal thrusts possibly extend further to the north than these scarps, in which case the scarps could might represent splay faults from a frontal thrust at depth. However we reinforce that the true extent of this signal is difficult to resolve and interpret from the InSAR time-series due to the overprinting of tectonic deformation by the subsidence along the KCIZ.

### 5.4 Considering additional model structural and rheological complexity

We explored the introduction of further complexity into our models. Solving for the position of the vertical strike-slip fault (Fig. S16) consistently shifts the location of the MKDF towards higher topography adjacent to the south of the fault. This is driven by a short wavelength reversal in the ascending LOS, which might be residual topographically correlated noise. This model also neglects the mapped surface position of the fault trace. Solving for the dip of the strike-slip fault is also possible, however outcrop exposures of the MKDF indicate a vertical fault at the near surface (Fig. S18) and the linear fault trace cutting through topography implies a vertical fault at depth.

There is evidence for vertical motion along the strike-slip fault (Figs 5). This is supported by geomorphological analysis of a palaeo-rupture scarp which describes localized vertical motion along the strike-slip fault [although this is attributed to variations in fault strike; Dodds *et al.* (2021)]. We model this following the approach of Daout *et al.* (2016a), in which dip-slip motion along the frontal thrust is conserved (Fig. S17). We model this be adding dip-slip motion on the vertical fault and imposing the shortening along the three structures to be conserved. This allows for the deep-seated convergence across the fault system to be partitioned between dip-slip motion on the frontal thrust fault and the strike-slip fault, such that the velocities are controlled by the geometry of the fault system and represent long-term deformation rates. This fits the resolved deformation in the LOS well, however the additional structural complexity does not significantly alter the posterior distribution of parameters. Furthermore dip-slip motion on a vertical fault is unlikely and instead might represent the inelastic vertical deformation of the hanging wall.

Introducing structural complexity into the models also neglects expected rheological heterogeneity either side of the MKDF. The MKDF separates the heavily deformed Iranian Plateau from the stable continental interior of the Turan Platform. The mechanical properties of these two regions are expected to be very different, which is reflected in the distribution of seismicity and topography (e.g. Jackson *et al.* 2002; Copley & Jackson 2006). The widespread folding and faulting in the Iranian Plateau suggests that it is comprised of material with much lower rigidity, in comparison to the Turan Platform (e.g. Maggi *et al.* 2000; Maggi & Priestley 2005). Further evidence for elastic heterogeneity across the MKDF is suggested by observations from the propagation of seismic waves from large earthquakes in the region. (Ambraseys 1997) demonstrated that throughout the historical record, earthquakes in this region have shown an asymmetry in their shaking intensity and damage distribution that extends far to the north but is limited to the south, possibly due to the difference in the elastic properties between the Köpetdag and Turan Platform.

InSAR observations of surface deformation on continental strike-slip faults can be used to probe rheological heterogeneity in the crust (e.g. Jolivet *et al.* 2008), with deformation concentrating on the more compliant side of the fault (e.g. Segall 2005). However with the MKDF, the inferred strain-partitioning immediately to the north of the fault combined with the anthropogenic degradation also

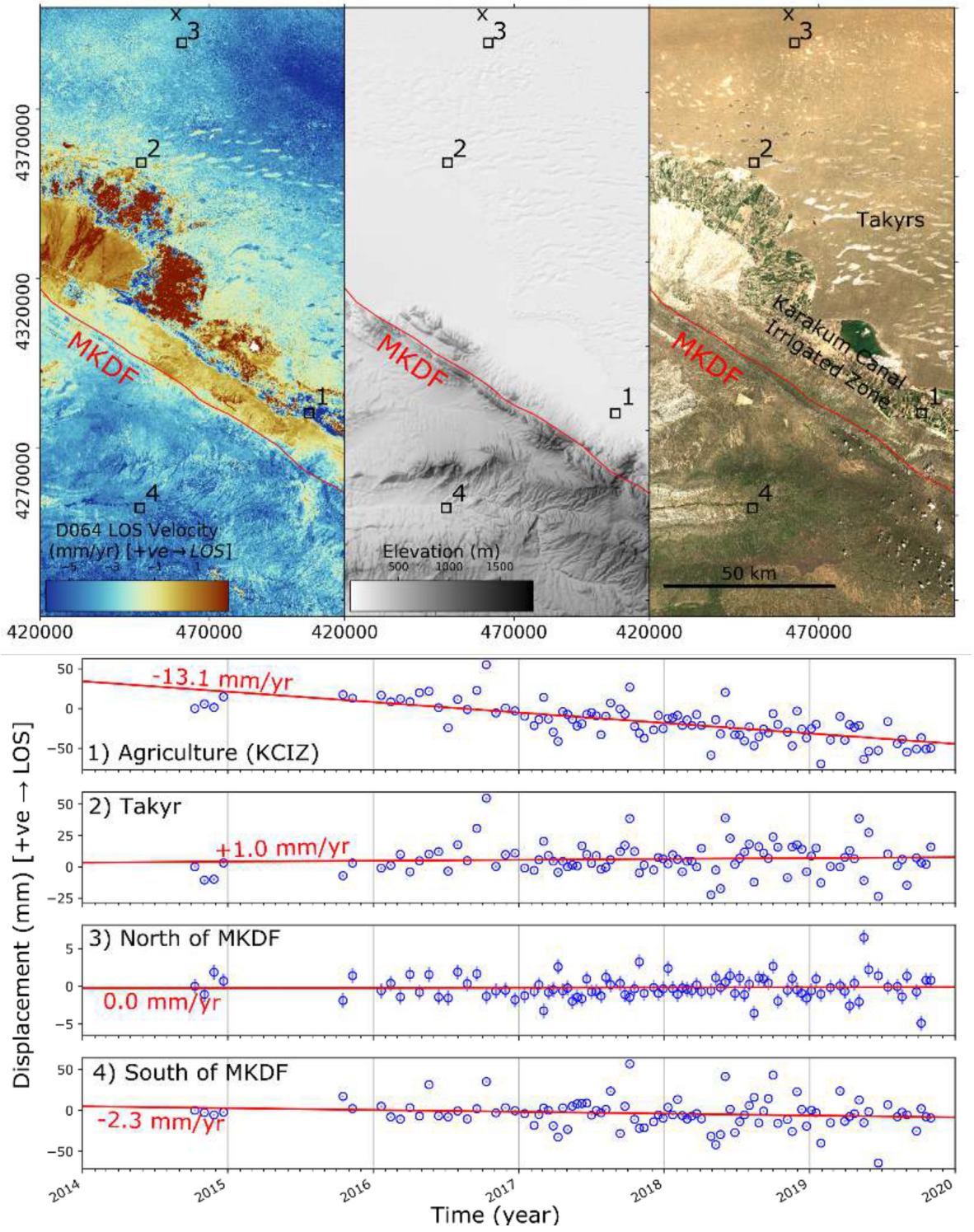


**Figure 7.** Upper map panels, from left to right: the time-series inversion from D064 (at the resolution of the unwrapped IFGs and prior to RMS masking); elevation and hillshade of the same area across the MKDF; Sentinel-2 optical imagery, with takyrs and the Karakum Canal irrigated zone visible (in UTM Zone 40 N). The lower panels are the cumulative displacement time-series of the points labelled 1–4 (square markers in the upper panels) from 2014 to 2020, referenced to the 'X' marker in north of the figure. Displacements are averaged over a 10 × 10 pixels, with the reference zone 100 × 100 pixels. The red line shows the linear fit (LOS velocity) to the displacement time-series (with no obvious seasonal trends).

in the near-field obscures any asymmetry. Nevertheless the rapid slip-rate combined with the remarkably linear fault trace for over 200 km suggests that the MKDF is representative of the localization to strain adjacent to a heterogeneity in crustal strength, as observed elsewhere in continental settings (e.g. Molnar & Dayem 2010).

### 5.5 Kinematics of the SCB

The Sentinel-1 InSAR time-series derived slip-rate (7.2 ± 2.4 mm yr$^{-1}$) and the geological slip-rate (9.1 ± 1.3 mm yr$^{-1}$; Walker *et al.* (2021)) are comparable within error. This implies the present rate of interseismic motion is consistent with the longer-term Quaternary rate. Taking the weighted mean of the geodetic and geological slip-rate, with an error $\sigma^2(\hat{\mu}) = \frac{1}{\sum \frac{1}{\sigma_i^2}}$, constrains the right-lateral motion along the MKDF to 8.7 ± 1.1 mm yr$^{-1}$.

Walker *et al.* (2021) revised an Iran–Eurasia–SCB velocity triangle from Copley & Jackson (2006) (after Jackson *et al.* 2002), to estimate the SCB is moving 10.4 ± 1.1 mm yr$^{-1}$ relative to Eurasia, in a direction 333° ± 5°. This is calculated assuming that conjugate strike-slip motion along the MKDF and SFZ accommodates the range-parallel component of motion of the SCB. The motion of Iran relative to stable Eurasia is constrained to 11.9 ± 0.4 mm yr$^{-1}$ in a direction of 358.5° using permanent GNSS stations in Central Iran (KHUR and MOBK; Khorrami *et al.* 2019). For the Iran-SCB vector, they use the the left-lateral motion along the SFZ (4.8 ± 0.8 mm yr$^{-1}$; 244°), derived from ascending and descending Envisat-InSAR time-series Mousavi *et al.* (2015). Walker *et al.* (2021) infer that because the eastern Alborz is accommodating shortening perpendicular to the SFZ, the Caspian vertex lies towards the centre of the triangle relative to this vector. Similarly, assuming the Köpetdag accommodates shortening perpendicular to the MKDF, the Caspian vertex must lie towards the interior of the triangle relative to this vector. The overlapping region between these vectors thus represents the plausible velocity for the SCB Walker *et al.* (2021).

We revise this velocity triangle further (Fig. 8), including the updated constraints of the motion accommodated by the MKDF. Instead of a pure right-lateral motion along the MKDF, we resolve a vector defined as the addition of the combined geodetic-geological fault-parallel slip-rate and the inverted range of fault-perpendicular shortening from our models. This estimates an oblique convergence vector of 9.7 ± 1.8 mm yr$^{-1}$ in a direction of 329 ± 9°. Instead of using the Envisat InSAR-derived rate from Mousavi *et al.* (2015) for the SFZ, we use the relative motion of permanent GNSS stations straddling the SFZ (BIAJ, $V_E$ 1.11 ± 0.28 mm yr$^{-1}$, $V_N$ 8.66 ± 0.22 mm yr$^{-1}$; MAVT, $V_E$ –4.80 ± 0.34 mm yr$^{-1}$, $V_N$ 5.78 ± 0.16 mm yr$^{-1}$; Mousavi *et al.* (2013). This also equates to a purely left-lateral slip vector across the SFZ with a slip-rate of 6.6 ± 0.8 mm yr$^{-1}$ in the direction 244 °. For Iran–Eurasia motion, we use 11.5 ± 0.1 mm yr$^{-1}$ in a direction of 001° from GNSS station KHUR (55.1°E; Khorrami *et al.* 2019). We note that the velocity of a GNSS station at 55°E might not be entirely representative of Iran–Eurasia convergence across the conjugate system (56–58°E), as GNSS velocities show an eastward reduction in the rate of convergence of ≈–1.2 mm yr$^{-1}$ per °E between 52 and 60°E (Khorrami *et al.* 2019).

The updated velocity triangle (Fig. 8) supports the rates and direction of motion for the SCB from Jackson *et al.* (2002), Copley & Jackson (2006) and Walker *et al.* (2021), approximately aligning with SCB–Eurasia vector from Walker *et al.* (2021) (10.4 ± 1.1 mm yr$^{-1}$ in a direction of 333° ± 5°). The primary difference

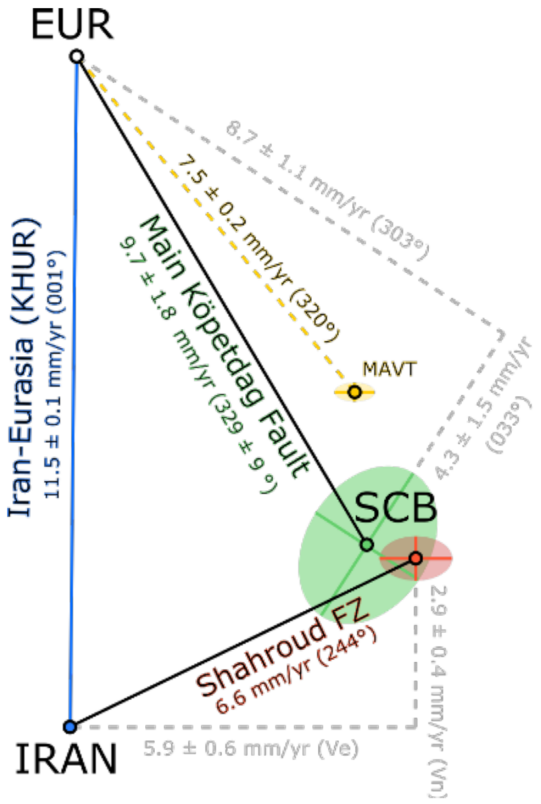


**Figure 8.** Velocity triangle constructed following Walker *et al.* (2021) for the relative motion of the South Caspian Basin, Eurasia and Iran. We resolve a vector for SCB–Eurasia motion from the combined measurement for strike-slip motion and our inverted range of shortening across the MKDF; 9.3 mm yr$^{-1}$ in a direction of 330° (green, error given by the ellipse). The relative motion of permanent GNSS stations located either side of the the Shahroud fault zone constrains SCB–Iran motion (Mousavi *et al.* 2013); 6.6 mm yr$^{-1}$ in the direction 244° (red). For the Iran-Eurasia vector at this longitude, we use GNSS station KHUR [blue, 11.5 ± 0.1 mm yr$^{-1}$, 001°; Khorrami *et al.* (2019)]. The velocity of GNSS station MAVT (possibly located on the SCB) relative to stable Eurasia is also shown (yellow).

is that the overlapping zones of the error ellipses suggests that motion along the conjugate MKDF-SFZ accommodates the motion of the SCB, without requiring much additional deformation within the East Caspian Lowlands or at the margins of the SCB in the eastern Alborz. However assuming the GNSS velocity of station MAVT is correct, the inverted rate of fault-perpendicular shortening is possibly slightly overestimated along the frontal thrusts. As discussed above, it is difficult to precisely constrain this motion due to the overprinting by non-tectonic deformation along the KCIZ. Nevertheless the inferred uplift signal to the north of the MKDF does correlate with the projected GNSS velocity of MAVT when considering the range of uncertainty in our models. This implies that the projected fault-perpendicular motion measured with GNSS in the East Caspian Lowlands is transferred to the frontal thrusts of the MKDF, rather than being distributed across structures in the East Caspian Lowlands.

## 6 CONCLUSION

We measure interseismic deformation along the MKDF with descending and ascending Sentinel-1 InSAR time-series. This implements a processing strategy for the simultaneous correction and

performance analysis of tropospheric models, which suggests a 25–40 per cent underestimation in the amplitude of the tropospheric path delay in this region. We model the fault-parallel motion across the MKDF, and combine this with the geological rate from Walker *et al.* (2021), to constrain $9 \pm 1$ mm yr$^{-1}$ right-lateral motion and a shallow locking depth of ≈6 km. We resolve a broad zone of decreased phase delay adjacent to the north of the MKDF, which we propose results from uplift along frontal thrusts. We model this using a strain-partitioning geometry which estimates $4 \pm 2$ mm yr$^{-1}$ of shortening across the frontal thrusts. This implies that convergence measured with GNSS in the East Caspian Lowlands is transferred to the frontal thrusts north of the MKDF (Mousavi *et al.* 2013). Revising velocity triangles from Walker *et al.* (2021) supports their proposed rate of motion for the SCB ($10 \pm 2$ mm yr$^{-1}$ in a direction of $330 \pm 10°$). However our models suggest that motion along the conjugate MKDF-SFZ is representative of the motion of the SCB, without requiring internal deformation of the SCB in the East Caspian Lowlands. Reconciling the inverted rate of shortening with GNSS velocities suggests that this is slightly overestimated, probably due to overprinting of tectonic signals along the Karakum Canal irrigated zone. Nevertheless, modelling the observed deformation with a strain-partitioning geometry implies that at this latitude (56–58°E) remaining Iran–Eurasia convergence is transferred to frontal thrusts to the north of the MKDF.

## ACKNOWLEDGMENTS

We would like thank both the editor, Andrew Barbour, and both reviewers, Jack Loveless and Anonymous, for their constructive comments which improved the manuscript.

This research is supported by the UK National Environment Research Council (NERC; Doctoral Training Partnership in Environmental Research; NE/L002612/1), the NERC-funded Centre for Observation and Modelling of Earthquakes, Volcanoes and Tectonics (COMET), the NERC grant 'Looking into the Continents from Space' (LiCS; NE/K011006/1), the NERC-ESRC Increasing Resilience to Natural Hazards program 'Earthquakes without Frontiers (EwF)' (NE/J02001X/1), by the Leverhulme Trust Research Project Grant 'EROICA' (RPG-2018-371) and the Global Challenge Research Fund (Internal Oxford QR allocation).

## DATA AVAILABILITY

InSAR data are provided by the ESA Copernicus Sentinel-1 Satellite Mission (scihub.copernicus.eu). InSAR time-series processing and analysis uses the NSBAS processing chain (forge.osug.fr). Tropospheric path-delay corrections are provided by the Generic Atmospheric Correction Online Service for InSAR (GACOS; www.gacos.net), with data from the European Centre for Medium-Range Weather Forecasts (ECMWF; operational high-resolution tropospheric products). LOS velocity fields are provided as electronic supplements (.grd files for both descending and ascending LOS at 250 m resolution in UTM Zone 40N; included are the average velocity, standard error, LOS heading and LOS incidence data sets).

## REFERENCES

Ambraseys, N.N., 1997. The Krasnovodsk (Turkmenistan) Earthquake of 8 July 1895, *J. Earthq. Eng.,* **1**(2), 293–317.

Ambraseys, N.N. & Melville, C.P., 2005. *A History of Persian Earthquakes,* Cambridge Univ. Press.

Ansari, H., De Zan, F. & Parizzi, A., 2020. Study of systematic bias in measuring surface deformation with SAR interferometry, *IEEE Trans. Geosci. Rem. Sens.,* **59**(2), 1285–1301.

Béjar-Pizarro, M., Socquet, A., Armijo, R., Carrizo, D., Genrich, J. & Simons, M., 2013. Andean structural control on interseismic coupling in the North Chile subduction zone, *Nat. Geosci.,* **6,** 462–467.

Bekaert, D.P., Hooper, A. & Wright, T.J., 2015. A spatially variable power law tropospheric correction technique for InSAR data, *J. geophys. Res.,* **120**(2), 1345–1356.

Berberian, M. & Yeats, R.S., 2001. Contribution of archaeological data to studies of earthquake history in the Iranian Plateau, *J. Struct. Geol.,* **23**(2–3), 563–584.

Chen, J., Zebker, H.A. & Knight, R., 2015. A persistent scatterer interpolation for retrieving accurate ground deformation over InSAR-decorrelated agricultural fields, *Geophys. Res. Lett.,* **42**(21), 9294–9301.

Copley, A. & Jackson, J., 2006. Active tectonics of the Turkish-Iranian Plateau, *Tectonics,* **25**(6), 1–19.

Daout, S. *et al.*, 2016b. Along-strike variations of the partitioning of convergence across the Haiyuan fault system detected by InSAR, *J. geophys. Int.,* **205**(1), 536–547.

Daout, S., Barbot, S., Peltzer, G., Doin, M.P., Liu, Z. & Jolivet, R., 2016a. Constraining the kinematics of metropolitan Los Angeles faults with a slip-partitioning model, *Geophys. Res. Lett.,* **43**(21), 11 192–11 201.

Daout, S., Dini, B., Haeberli, W., Doin, M.P. & Parsons, B., 2020. Ice loss in the Northeastern Tibetan Plateau permafrost as seen by 16 yr of ESA SAR missions, *Earth planet. Sci. Lett.,* **545,**.

Daout, S., Doin, M.P., Peltzer, G., Lasserre, C., Socquet, A., Volat, M. & Sudhaus, H., 2018. Strain partitioning and present-day fault kinematics in NW Tibet from Envisat SAR interferometry, *J. geophys. Res.,* **123**(3), 2462–2483.

Djamour, Y. *et al.*, 2010. GPS and gravity constraints on continental deformation in the Alborz mountain range, Iran, *J. geophys. Int.,* **183**(3), 1287–1301.

Dodds, N., Begenjev, G., Bezmenov, Y., Gruetzner, C., Mirzin, R., Rhodes, E., Walker, R. & Wordsworth, P., 2021. *A Large-Magnitude Medieval Earthquake on the Main Köpetdag (Kopeh Dagh) Fault,* Turkmenistan, in press.

Doin, M.-P. *et al.*, 2011. Presentation of the small baseline NSBAS processing chain on a case example: the Etna deformation monitoring from 2003 to 2010 using Envisat data, in *Proceedings of the ESA 'Fringe 2011 Workshop',* Frascati, Italy.

Doin, M.P., Lasserre, C., Peltzer, G., Cavalié, O. & Doubre, C., 2009. Corrections of stratified tropospheric delays in SAR interferometry: validation with global atmospheric models, *J. Appl. Geophys.,* **69**(1), 35–50.

Doin, M.P., Twardzik, C., Ducret, G., Lasserre, C., Guillaso, S. & Jianbao, S., 2015. InSAR measurement of the deformation around Siling Co Lake: inferences on the lower crust viscosity in central Tibet, *J. geophys. Res.* **120** 7 5290–5310

Ekström, G., M. Nettles, and A. M. Dziewonski(2012) The global CMT project 2004-2010: Centroid-moment tensors for 13,017 earthquakes *Phys. Earth Planet. Inter.* **200**

Elliott, J.R., Biggs, J., Parsons, B. & Wright, T.J., 2008. InSAR slip rate determination on the Altyn Tagh Fault, northern Tibet, in the presence of topographically correlated atmospheric delays, *Geophys. Res. Lett.,* **35**(12), 1–5.

Goldstein, R.M. & Werner, C.L., 1998. Radar interferogram filtering for geophysical applications, *Geophys. Res. Lett.,* **25**(21), 4035–4038.

Grandin, R., 2015. Interferometric processing of SLC Sentinel-1 TOPS data, in *European Space Agency,* Special Publication ESA SP.

Grandin, R., Doin, M.P., Bollinger, L., Pinel-Puysségur, B., Ducret, G., Jolivet, R. & Sapkota, S.N., 2012. Long-term growth of the Himalaya inferred from interseismic InSAR measurement, *Geology,* **40**(12), 1059–1062.

Grandin, R., Klein, E., Métois, M. & Vigny, C., 2016. Three-dimensional displacement field of the 2015 Mw8.3 Illapel earthquake (Chile) from across- and along-track Sentinel-1 TOPS interferometry, *Geophys. Res. Lett.,* **43**(6), 2552–2561.

Hanssen, R.F., 2001. *Radar Interferometry: Data Interpretation and Error Analysis: 2 (Remote Sensing and Digital Image Processing),* Springer.

Hollingsworth, J. *et al.*, 2010. Active tectonics of the east Alborz mountains, NE Iran: Rupture of the left-lateral Astaneh fault system during the great 856 A.D. Qumis earthquake, *J. geophys. Res.,* **115**(12), 1–19.

Hollingsworth, J., Jackson, J., Walker, R., Gheitanchi, M.R. & Bolourchi, M.J., 2006. Strike-slip faulting, rotation, and along-strike elongation in the Kopeh Dagh mountains, NE Iran, *J. geophys. Int.,* **166,** 1161–1177.

Hollingsworth, J., Jackson, J., Walker, R. & Nazari, H., 2008. Extrusion tectonics and subduction in the easter South Caspian region since 10 Ma, *Geology,* **36**(10), 763–766.

Jackson, J., Priestley, K., Allen, M. & Berberian, M., 2002. Active tectonics of the South Caspian Basin, *J. geophys. Int.,* **148,** 214–245.

Javidfakhr, B., Bellier, O., Shabanian, E., Siame, L., Léanni, L., Bourlès, D. & Ahmadian, S., 2011. Fault kinematics and active tectonics at the southeastern boundary of the eastern Alborz (Abr and Khij fault zones): Geodynamic implications for NNE Iran, *J. Geodyn.,* **52**(3), 290–303.

Jolivet, R., Cattin, R., Chamot-Rooke, N., Lasserre, C. & Peltzer, G., 2008. Thin-plate modeling of interseismic deformation and asymmetry across the Altyn Tagh fault zone, *Geophys. Res. Lett.,* **35**(2), 1–5.

Jolivet, R., Grandin, R., Lasserre, C., Doin, M.P. & Peltzer, G., 2011. Systematic InSAR tropospheric phase delay corrections from global meteorological reanalysis data, *Geophys. Res. Lett.,* **38**(17), 1–6.

Khorrami, F. *et al.*, 2019. An up-to-date crustal deformation map of Iran using integrated campaign-mode and permanent GPS velocities, *J. geophys. Int.,* **217**(2), 832–843.

López-Quiroz, P., Doin, M.P., Tupin, F., Briole, P. & Nicolas, J.M., 2009. Time series analysis of Mexico City subsidence constrained by radar interferometry, *J. appl. Geophys.,* **69**(1), doi:10.1016/j.jappgeo.2009.02.006.

Lyberis, N. & Manby, G., 1999. Oblique to orthogonal convergence across the Turan Block in the Post-Miocene, *AAPG Bull.,* **83**(7), 1135–1160.

Maggi, A., Jackson, J.A., McKenzie, D. & Priestley, K., 2000. Earthquake focal depths, effective elastic thickness, and the strength of the continental lithosphere, *Geology,* **28**(6), 495–498.

Maggi, A. & Priestley, K., 2005. Surface waveform tomography of the Turkish-Iranian plateau, *J. geophys. Int.,* **160**(3), 1068–1080.

Masson, F., Anvari, M., Djamour, Y., Walpersdorf, A., Tavakoli, F., Daignières, M., Nankali, H. & Van Gorp, S., 2007. Large-scale velocity field and strain tensor in Iran inferred from GPS measurements: new insight for the present-day deformation pattern within NE Iran, *J. geophys. Int.,* **170**(1), 436–440.

Maubant, L. *et al.*, 2020. Independent component analysis and parametric approach for source separation in InSAR time series at regional scale: application to the 2017–2018 slow slip event in Guerrero (Mexico), *J. geophys. Res.,* **125**(3), 1–24.

McKenzie, D., 1972. Active tectonics of the Mediterranean region, *Geophys. J. R. Astron. Soc.,* **30**(2), 109–185.

Molnar, P. & Dayem, K.E., 2010. Major intracontinental strike-slip faults and contrasts in lithospheric strength, *Geosphere,* **6**(4), 444–467.

Mousavi, Z., Pathier, E., Walker, R.T., Walpersdorf, A., Tavakoli, F., Nankali, H., Sedighi, M. & Doin, M.P., 2015. Interseismic deformation of the Shahroud fault system (NE Iran) from space-borne radar interferometry measurements, *Geophys. Res. Lett.,* **42**(14), 5753–5761.

Mousavi, Z., Walpersdorf, A., Walker, R.T., Tavakoli, F., Pathier, E., Nankali, H., Nilfouroushan, F. & Djamour, Y., 2013. Global positioning system constraints on the active tectonics of NE Iran and the South Caspian region, *Earth planet. Sci. Lett.,* **377–378,** 287–298.

Murray, K.D., Bekaert, D.P. & Lohman, R.B., 2019. Tropospheric corrections for InSAR: statistical assessments and applications to the Central United States and Mexico, *Rem. Sens. Environ.,* **232**(July), 111326 , doi:10.1016/j.rse.2019.111326.

O'Hara, S.L., 1997. Irrigation and land degradation: implications for agriculture in Turkmenistan, central Asia, *J. Arid Environ.,* **37**(1), 165–179.

Pinel-Puysségur, B., Michel, R. & Avouac, J.P., 2012. Multi-link InSAR time series: enhancement of a wrapped interferometric database, *IEEE J. Select. Top. Appl. Earth Observ. Rem. Sens.,* **5**(3), doi:10.1109/JSTARS.2012.2196758.

Rosen, P.A., Hensley, S., Peltzer, G. & Simons, M., 2004. Updated repeat orbit interferometry package released, **85**(53), 47.

Savage, J.C. & Burford, R.O., 1973. Geodetic determination of relative plate motion in central California, *J. geophys. Res.,* **78**(5), 832–845.

Segall, P., 2005. *Earthquake and Volcano Deformation,* Princeton Univ. Press.

Shabanian, E., Bellier, O., Siame, L., Arnaud, N., Abbassi, M.R. & Cochemé, J.J., 2009a. New tectonic configuration in NE Iran: active strike-slip faulting between the Kopeh Dagh and Binalud mountains, *Tectonics,* **28**(5), 1–29.

Shabanian, E., Siame, L., Bellier, O., Benedetti, L. & Abbassi, M.R., 2009b. Quaternary slip rates along the northeastern boundary of the Arabia-Eurasia collision zone (Kopeh Dagh Mountains, Northeast Iran), *J. geophys. Int.,* **178**(2), 1055–1077.

Shen, L., Hooper, A. & Elliott, J., 2019. A spatially varying scaling method for InSAR tropospheric corrections using a high-resolution weather model, *J. geophys. Res.,* **124**(4), 4051–4068.

Storchak, D.A., D. Di Giacomo, I. Bondár, E.R. Engdahl, J. Harris, W.H.K. Lee, A. Villaseñor and P. Bormann (2013) Seismological Research Letters *810.*, 0895-0695

Sudhaus, H. & Jónsson, S., 2009. Improved source modelling through combined use of InSAR and GPS under consideration of correlated data errors: application to the June 2000 Kleifarvatn earthquake, Iceland, *J. geophys. Int.,* **176**(2), 389–404.

Tchalenko, J.S. & Skempton, A.W., 1975. Seismicity and structure of the Kopet Dagh, *Phil. Trans. R. Soc. Lond., A,* **278**(1275), 1–28.

Trifonov, V.G., 1978. Late Quaternary tectonic movements of western and central Asia, *GSA Bull.,* **89**(7), 1059–1072.

Tymofyeyeva, E. & Fialko, Y., 2015. Mitigation of atmospheric phase delays in InSAR data, with application to the eastern California shear zone, *J. geophys. Res.,* **120**(8), 5952–5963.

Van Dijk, J. *et al.*, 2019. An integrated geological model for the greater Cheleken area central Caspian Basin, Turkmenistan; complex synsedimentary transcurrent faulting and compartmentalization in Plio-Pleistocene clastic reservoirs, in *Society of Petroleum Engineers - Abu Dhabi International Petroleum Exhibition and Conference 2018, ADIPEC 2018,* pp. 0–9.

Vergne, J., Cattin, R. & Avouac, J.P., 2001. On the use of dislocations to model interseismic strain and stress build-up at intracontinental thrust faults, *J. geophys. Int.,* **147**(1), 155–162.

Walker, R.T. *et al.*, 2021. Slip-rate on the Main Kopetdag (Kopeh Dagh) Strike-slip fault, Turkmenistan, and the active tectonics of the South Caspian, *Tectonics,* **40**(8), doi:10.1029/2021TC006846.

Walters, R.J., Elliott, J.R., Li, Z. & Parsons, B., 2013. Rapid strain accumulation on the Ashkabad fault (Turkmenistan) from atmosphere-corrected InSAR, *J. geophys. Res.,* **118**(7), 3674–3690.

Weatherall, P. *et al.*, 2015. A new digital bathymetric model of the world's oceans, *Earth Space Sci.,* **2**(8), 331–345.

Weiss, J.R. *et al.*, 2020. High-resolution surface velocities and strain for Anatolia from Sentinel-1 InSAR and GNSS data, *Geophys. Res. Lett.,* **47**(17), e2020GL087376 , doi:10.1029/2020GL087376.

Wimpenny, S., 2020. Global Waveform Catalogue (gWFM) v1.0, doi:10.5281/zenodo.3782608.

Xu, X., Sandwell, D.T., Klein, E. & Bock, Y., 2021. Integrated Sentinel-1 InSAR and GNSS time-series along the San Andreas Fault System, *J. geophys. Res.,* **126**(11), e2021JB022579.

Yu, C., Li, Z. & Penna, N.T., 2018a. Interferometric synthetic aperture radar atmospheric correction using a GPS-based iterative tropospheric decomposition model, *Rem. Sens. Environ.,* **204**(October 2017), 109–121.

Yu, C., Li, Z., Penna, N.T. & Crippa, P., 2018b. Generic atmospheric correction model for interferometric synthetic aperture radar observations, *J. geophys. Res.,* **123**(10), 9202–9222.

Yu, C., Penna, N.T. & Li, Z., 2017. Generation of real-time mode high-resolution water vapor fields from GPS observations, *J. geophys. Res.,* **122**(3), 2008–2025.

## SUPPORTING INFORMATION

Supplementary data are available at *GJI* online.

**Table S1**. Previous estimates of the rate of interseismic motion on the MKDF from a variety of methods. The slip-rate estimates are highly variable and inconsistent within uncertainty bounds.
**Figure S1**. Descending track D064 perpendicular baseline versus temporal baseline plot. The InSAR time-series consists of 290 IFGs from 96 acquisitions.
**Figure S2**. Ascending track A159 perpendicular baseline versus temporal baseline plot. The InSAR time-series consists of 392 IFGs from 126 acquisitions.
**Figure S3**. Correcting IFGs with an empirical phase-elevation relationship (a) 20141127–20150207, (b) 20150619–20150713; from D064). The phase-elevation correction is good at capturing the relationship with topography in the lower right of both IFGS; however in both cases large turbulent stratospheric delays in the low elevation region to the north remain after the correction and dominate the corrected IFG.
**Figure S4**. InSAR time-series for D064 without atmospheric corrections (using the time-series ramp-tying method explained in this paper). Red cross to the north is the reference area (100 × 100 pixels), chosen to be in the far field from the fault at low elevation. The displacement time-series of numbered pixels 0–3 (averaging across 20 × 20 pixels) are shown below, with the red lines showing the decomposed linear trend for the velocity maps. These aim to capture different areas in the time-series to resolve possible seasonality in the time-series: 0) Karakum Canal irrigated zone, (1) takyrs, (2) low elevation and (3) high elevation. We are unable to solve for a robust seasonal signal in the time-series maps due to the influence of turbulent signals dominating the time-series which results in high perturbances from any seasonal trend in the time-series.
**Figure S5**. Left-hand panel: tropospheric path-delay correction with GACOS for IFG 20171229–20180311, with the processing strategy presented above. Right-hand panel: $\phi_{\mathrm{GACOS}}$ versus $\phi_{\mathrm{IFG}} - \phi_{\mathrm{RAMP}}$ plot, coloured by elevation. This demonstrates an example where the GACOS model corresponds to the IFG phase excellently. The statistical metrics reflect this observation. Both the gradient of the $\phi_{\mathrm{GACOS}}$ versus $\phi_{\mathrm{IFG}} - \phi_{\mathrm{RAMP}}$ are very close to 1; the correction results in standard deviation reduction of ≈45 per cent.
**Figure S6**. Left-hand panel: tropospheric path-delay correction with GACOS for IFG 20161104–2016122, with the processing strategy presented above. Right-hand panel: $\phi_{\mathrm{GACOS}}$ versus $\phi_{\mathrm{IFG}} - \phi_{\mathrm{RAMP}}$ plot, coloured by elevation. This is an example that relates to the histogram results for the entire time-series. The distribution of the $\phi_{\mathrm{GACOS}}$ versus $\phi_{\mathrm{IFG}} - \phi_{\mathrm{RAMP}}$ plot remains linear however the gradient is only 0.73. This contrasts with the correlation, which is excellent (>0.9). This suggests that the spatial pattern of the corrections are excellent, however the amplitude of the corrections is underestimating the phase-delay by >25 per cent.
**Figure S7**. Left-hand panel: tropospheric path-delay correction with GACOS for IFG 20181212–20190105, with the processing strategy presented above. Right-hand panel: $\phi_{\mathrm{GACOS}}$ versus $\phi_{\mathrm{IFG}} - \phi_{\mathrm{RAMP}}$ plot, coloured by elevation. This presents an example where the GACOS correction is not performing satisfactorily, highlighted by low performance in all three statistical metrics. This example reinforces the benefit of the simultaneous ramp estimation between the IFG phase and the model phase. Despite the difficulty with turbulent tropospheric signals, the corrected IFG still has a reduced variance when compared with the uncorrected IFG.
**Figure S8**. Top row: LOS velocity rate-maps from time-series inversion for the descending (left-hand panel) and ascending (right-hand panel) tracks (LOS velocity in mm yr$^{-1}$, with positive motion towards the LOS direction of the satellite). MKDF is delineated by a solid black line, striking WNW–ESE. Bottom row: corresponding 1$\sigma$ uncertainty (in mm yr$^{-1}$) maps from the time-series inversion for D064 (left-hand panel) and A159 (right-hand panel).
**Figure S9**. Schematic of the expected LOS observations from right-lateral motion along the MKDF, observed in the descending and ascending LOS; red/orange colours represent motion of the ground towards the LOS, blue away from the LOS. (a) Descending LOS; (b) Ascending LOS. Panels (c) and (d) are the same as the panels above, except for the addition of a thrust fault to the north of the MKDF. This structure results in uplift to the north of the MKDF, which is difficult to distinguish in the descending LOS as the signal is additive. However in the ascending LOS, the uplift signal opposes this motion and is more obvious in the LOS.
**Figure S10**. Investigating the potential effects of short baseline interferogram biases on the results of the time-series inversion with comparison maps for D064. Top row, from left to right: including IFGs with short baselines; excluding IFGs with temporal baselines ≤12 d (the eventual network used for analysis in this paper); the best-fitting ramp ($ax + by + c$) from a simultaneous inversion of the two time-series inversions; the residual difference of the time-series including the estimated ramp. No short baseline biases that might affect the interpretation of tectonic signals are observed for this region of the Köpetdag. Bottom row, left: histogram plot of the residual showing the zero-centred mean and standard deviation (affected by extreme outliers). Bottom row, right: plotting the residual velocity versus elevation; there is no discernible phase-elevation relationship.
**Figure S11**. Empirical covariance estimation for the D064 following the method of Sudhaus & Jonsson (2009). Estimation uses the functional form $b\exp(\frac{-h}{a})$. The autovariance ($b$) is ≈0.10 mm$^2$ and e-folding decay length scale ($a$) is ≈270 m.
**Figure S12**. Modelling the descending LOS time-series data from three profiles (MKD5–7) yields variable results for the rate of right-lateral strike-slip motion the MKDF. With profile lengths ≤100 km, there is a systematic increase in the slip-rate, due to near fault signals resolved in the LOS. A similar behaviour is observed for profile lengths ≥180 km (much greater than the typical wavelength of deformation for a continental strike-slip fault). Therefore we confine our modelling analysis to profile lengths of 120–160 km to mitigate this behaviour. Nevertheless, the rate of strike-slip motion is constrained to within 7 ± 2 mm yr$^{-1}$ along the MKDF.
**Figure S13**. Decomposition of the LOS velocity fields into a fault parallel (135°, left-hand panel) and vertical component (right-hand panel). LOS data is downsampled to a 250 m grid prior to the decomposition, and re-referenced to the far north of the overlap of the LOS velocity fields. Right-lateral strike-slip motion along the MKDF is visible in the fault-parallel component, as well as inferred uplift adjacent to the north of the MKDF in the vertical component.
**Figure S14**. Modelling the surface deformation in profile MKD5 (120 km length, 20 km width). (a) Inverting the surface deformation in only the descending LOS. (b) Inverting the surface deformation in both the descending and ascending LOS. We do not model the surface deformation with a more complex geometry due to the wide zone of overprinting by the Karakum Canal irrigated zone (in comparison to Fig. 6).

**Figure S15**. Modelling profile MKD7 (120 km length, 20 km width) with the same approach as Fig. 6(a–c). In panel (c) it is difficult to constrain the precise horizontal extent of the thrust fault to the North due to the overprinting width of ≈10 km of the Karakum Canal irrigated zone.

**Figure S16**. Introducing an additional free parameter to the inversion, the location of the primary strike-slip fault ($D_{SS}$). The topography shown is a sliding median of the topography with a window size of 1 km. The topographic ridge (the northernmost in the Köpetdag) is aligned with the strike of the MKDF, although offset by 1–5 km to the south. Interpreting the near-field signals with this model is difficult due the variability along strike of the position of the MKDF and the topographic ridge within a profile. Both of these have a variation of several kilometres within each profile swath. This model is likely affected by residual topographically correlated deformation signals, and also neglects the mapped surface trace position of the strike-slip MKDF.

**Figure S17**. Modelling the surface deformation with a fixed position strike-slip fault and thrust fault extending northward, with the addition of the conservation of motion on the frontal thrust. This geometry results in vertical motion directly above the strike-slip fault. There is evidence along the MKDF for localized vertical motion, however this model does not account for permanent inelastic deformation (e.g. anticlines) between the strike-slip and frontal thrust faults.

**Figure S18**. Fault cross-section exposure from a gravel quarry that has recently excavated across the fault (location: 38.40091°N, 57.36005°E), photographed during a field campaign to Turkmenistan in November 2019. The near-surface fault exposure (≈5 m) is dipping vertically, as expected for a relatively mature, strike-slip fault. This provides evidence to reinforce modelling the MKDF as a vertical structure.